
Article:
Sun, Y., Zhao, D., Ni, S. et al. (2 more authors) (2020) Entropy and flame transfer function analysis of a hydrogen-fueled diffusion flame in a longitudinal combustor. Energy, 194. ISSN 0360-5442

https://doi.org/10.1016/j.energy.2019.116870

Entropy and Flame Transfer Function Analysis of a Hydrogen-Fueled Diffusion Flame in a Longitudinal Combustor

Yuze Sun[1], Dan Zhao[1]*, Siliang Ni[1], Tim David[1], Yang Zhang[2]

[1]*Department of Mechanical Engineering, College of Engineering, University of Canterbury, Private Bag 4800, Christchurch 8041, New Zealand.*

[2]*Department of Mechanical Engineering, the University of Sheffield, Sheffield S1 3JD, UK*

Abstract: In this work, entropy generation and flame transfer function investigations are conducted on a hydrogen-burnt diffusion flame in a longitudinal combustor with acoustic waves present. For this, a time-domain 2D numerical model of a jet diffusion flame is developed to gain insights on its dynamic response to acoustic disturbances at either resonant or non-resonant frequencies. The model is validated first by comparing the numerical results such as turbulence intensities, pressure and velocity mode shape and flame shapes with the experimental data available in the literature. The model is then applied to evaluate the effects of the frequencies and amplitudes of the forcing acoustic waves, and the flame-holder/nozzle axial positions on entropy generation of both hydrogen- and propane-fueled flames. It is found that the entropy generation rate is sensitive to acoustic forcing frequencies, amplitudes and the nozzle axial positons. Furthermore, entropy produced from the heat conduction and the chemical reaction processes is shown to be dominant and secondary respectively. However, the mass diffusion is found to play a negligible role on entropy generation. As the acoustic forcing frequency is set to 385 Hz near resonance, the total entropy generation rates are minimized, and the mass diffusion contribution is maximized with the flame being placed at velocity node locations in comparison with other flame-holding locations. Finally, flame transfer function (FTF) analysis is performed by using two different methods. It is shown that the flame responds strongly to low-frequency acoustic disturbances, acting like a band-pass filter. Increasing the acoustic intensity leads to the flame being more sensitive to the acoustic disturbances over more frequency bands.

---

[1]*Corresponding author. Email: dan.zhao@canterbury.ac.nz (Dan Zhao)

Keywords: *Hydrogen; diffusion flame; entropy analysis; combustion instability; flame transfer function*

1. Introduction

Increasing concern about global energy and environmental issues leads to a resurgence of intensive research on hydrogen production and hydrogen-involved premixed or diffusion combustion in recent decades [1]. Compared to conventional hydrocarbon fuels, such as gasoline, diesel and fuel oil, hydrogen is relatively environmentally friendly [2, 3]. The full combustion of hydrogen leads to zero emissions of CO_2 and CO in theory. Thus, greenhouse gas emission produced is minimized [4, 5]. Due to these attractive features, hydrogen has great potential to be applied in modern power generation or propulsion systems, such as gas turbines and aero-engine [6, 7]. However, these modern systems are more susceptible to combustion instability [8], also known as thermo-acoustic instability [9]. When such an instability occurs, it can lead to flame extinction, overheating, engine structural vibration and even cause system failure [10, 11]. This undesirable instability phenomenon is believed to result from the dynamic interaction between acoustic waves and heat release perturbation in a combustion system [12, 13].

Extensive experimental, theoretical and numerical research on premixed and non-premixed flames under the acoustic excitation have been carried out in order to better understand and solve thermoacoustic instability problems [14-16]. Lieuwen [17, 18] provided an excellent review on premixed flame-acoustic wave interactions via the investigation of acoustic wave interactions with turbulent, premixed flames. Hwang et al. [19] performed experimental measurements on a dump combustor to study axial lengths and center lengths of a premixed ethylene-air flame affected by oncoming inlet velocity, equivalence ratio, and acoustic forcing. Kim et al. [20] conducted an experiment on a swirl-stabilized combustor to study combustion instability via examining the recirculation zones and vortex interaction. Fichera et al. [21] conducted both linear and non-linear analyses of thermo-acoustic instability on a methane-fueled lab-scale combustor. Khalil et al. [22]

examined heat release perturbation from a methane-burnt flame under the acoustic wave excitation in a swirl combustor. The flame stability and noise emission were the focus of their studies, which are important concerns for gas turbine applications. Singh et al. [23] performed both experimental and numerical studies on a swirl stabilized diffusion flame to study the thermo-acoustic behavior. Farhat et al. [24] performed experimental tests on a propane-burnt flame under the acoustic wave excitation in a longitudinal tube to study the flame characteristics. They showed that the diffusion propane-burnt flame could be involved with different structures and color, as the acoustic frequencies and nozzle positions changed. Chen et al. [25, 26] conducted detailed experimental research on the flame acoustic interaction of both premixed and diffusion propane-burnt flame. Experimental measurements were achieved by using Particle Image Velocimetry (PIV) to shed light on flow characteristics and the flame response to acoustic excitation.

Previous studies on flame-acoustics interaction attempt to reveal the relationship between heat release rates and velocity disturbances [27]. It has been shown that the unsteady heat release rates and velocity fluctuation are related and can be characterized by using flame transfer function s(FTF) [28, 29] or flame describing functions (FDF) [30]. These functions have been shown to be an effective tool to predict the flame response in an acoustically resonant combustor [31, 32]. Numerous researchers have performed FTF/FDF studies [33, 34]. For example, Balachandran et al. [31] studied the ethylene-air premixed experimentally and also measured the flame transfer function. Durox et al. [32] measured the flame transfer functions of different flame geometries experimentally. Karimi [33] also measured the flame transfer function through experiments in which a laminar premixed flame was studied under low amplitude acoustic excitation. Sabatino et al. [34] experimentally investigated the effect of acoustic pressure on the response of methane–air and propane–air swirl flames via determining the flame transfer functions (FTF). There are also a

number of numerical investigations on flame transfer function. Krediet et al. [35] identified the flame describing function (FDF) from a large eddy simulation (LES) of a swirled flame combustion system, in which the nonlinear response of a premixed flame was studied. Similar LES simulations are conducted in Ref. [36] to study the turbulent premixed flame in a swirl burner, in which the boundary conditions of combustion chamber wall are considered. Silva et al. [37] studied the thermoacoustic instability of a premixed flame via DNS (Direct Numerical Simulations). Chen et al. [38] numerically determined the FTF of a propane-fueled jet fusion flame in a longitudinal standing-wave combustor by applying acoustic disturbance consisting of a number of superimposed acoustic tones. However, this superimposition method could lead to 'numerical error' such as round off in comparison with the classical means of applying single-tone disturbances to excite the flame. However, previous studies did not provide comparison and validation of the FTF by using these two different methods. This was partially motivated the present work.

Entropy analysis is an alternative but effective approach to evaluate combustion processes and thermodynamics second-law performance of a thermal-fluid system [39]. In order to understand the exergy loss of the flame-acoustic interaction process, it is important to investigate the local entropy generation. There are many previous studies concerned with entropy generation. Nishida et al. [39] analyzed local entropy generation and exergy loss of both premixed and diffusion flames using the CHEMKIN program. Briones et al. [40] conducted a theoretical–numerical analysis to investigate the entropy generation of a laminar H_2-enriched CH_4–air flame. Jiang et al. [41] studied the entropy generation of H_2/air combustion processes effected by CO addition. Wang et al. [42] investigated a premixed flame with methane fuel but with hydrogen addition in a micro-planar combustor, in which multistep kinetics was used. Jiang et al. [43] performed numerical simulations

with the commercial software Fluent to analyze the entropy generation of a hydrogen-air premixed flame in micro-combustors. The effects of the baffles height, the inlet mass flow rate and the equivalence ratio was examined. The entropy generation and second law efficiency of turbulent non-premixed flame was numerically investigated in Refs. [44, 45] on a hydrogen- or methane-air combustor. The effects of the equivalence ratios and swirl numbers were examined. E et al. [46] performed a 3D simulation to investigate the effect of inlet pressure on the entropy destructive and exergy efficiency of a hydrogen-air premixed flame in a micro-combustor with a step. However, to the best knowledge of the authors, there is a lack of investigation in analyzing the entropy generation of hydrogen-fueled diffusion flame under the acoustic excitation in a longitudinal combustor. This was also partially motivated the present study.

In this work, numerical simulations are conducted to analyze the entropy generation and flame transfer function of a hydrogen-fueled diffusion flame under acoustic excitation. Comparison is then made between the hydrogen- and propane-fueled results. Emphasis is placed on evaluating the roles of 1) heat conduction, 2) mass diffusion and 3) chemical reaction processes in contributing the total entropy generation, as the acoustic frequencies and amplitudes, and the nozzle axial position are varied. The flame dynamic response is quantitatively examined by evaluating the flame transfer functions over a given frequency range. Two different numerical methods are applied and compared. The paper is organized as follows: the numerical model and governing equations are described in Sect. 2. Validation and benchmarking the model are conducted in Sect. 3. The entropy generation and flame transfer function results are discussed in Sect. 4. Key findings are summarized in Sect. 5.

2. Description of Numerical Model

2.1 Numerical model

The hydrogen-fueled combustion system with acoustic disturbances present is schematically illustrated in Fig. 1(a). This is consistent with the experimental rig (see Fig. 1(b)) on which flame dynamics measurements are conducted in Refs. [24, 38]. The combustion system involves 4 key components: a square tube, a jet nozzle to anchor the diffusion flame, a loudspeaker to produce acoustic disturbances and a cone-shaped connector between the square tube and the loudspeaker. The axial length of the square tube is 800 mm. Its upper end is acoustically open with cross-sectional dimensions of 114 (L) ×114 (W) mm whilst the connecting cone height is approximately 300 mm. The detailed dimensions of the combustion system are included in the caption of Fig. 1. Fig. 1(c) shows a structured mesh generated by using the Ansys workbench meshing (V18.2). The geometry is assumed to be axisymmetric and a graded mesh is applied in the neighborhood of the flame nozzle.

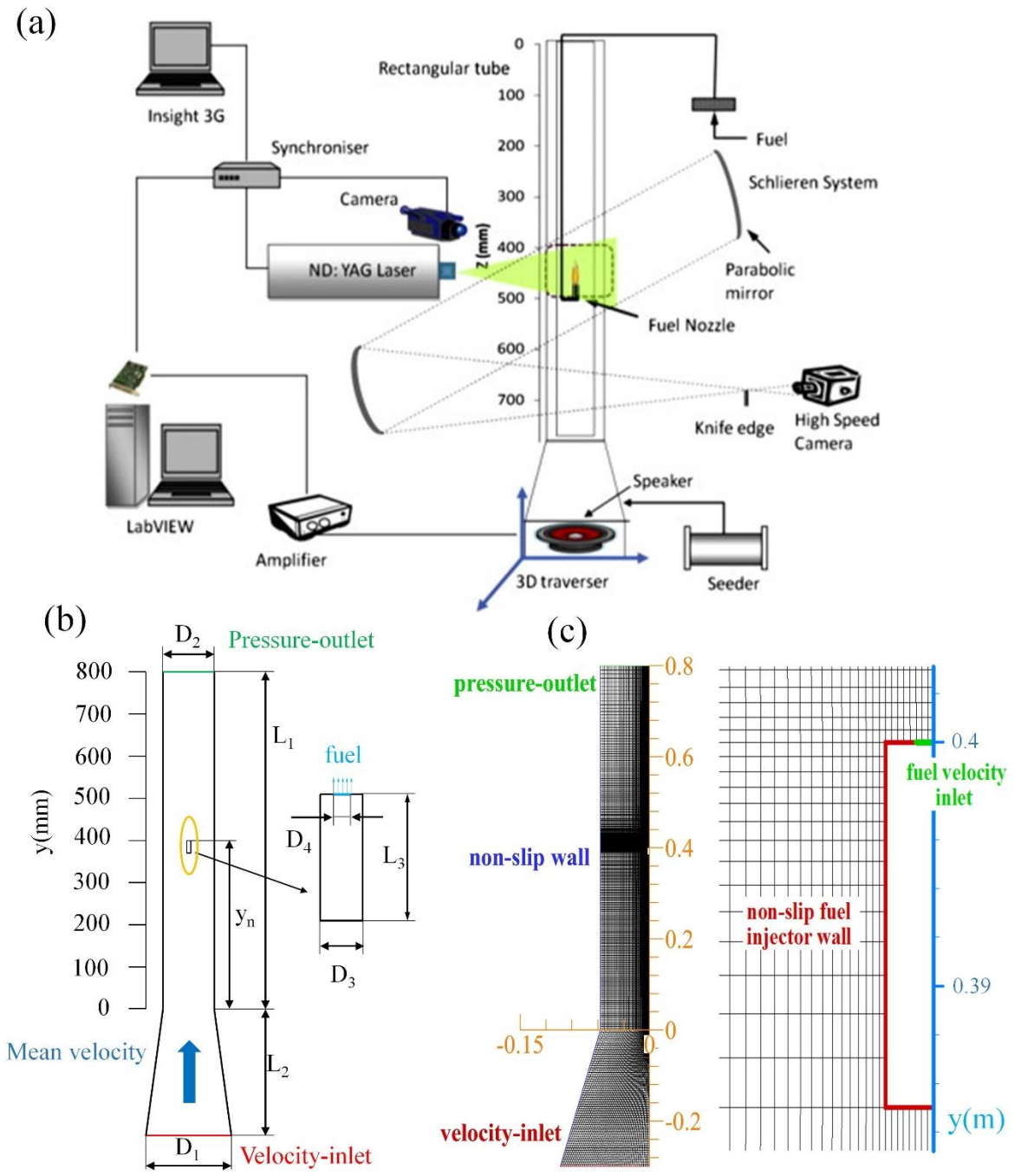

Fig. 1. (a) Drawing of the experimental setup [24, 38]. (b) Schematic of the numerical model (c) numerical mesh with a zoom-in graph near the nozzle. The dimensions of the modelled combustor are given as D_1=114.0 mm, D_2=207 mm, D_3=5.0 mm, D_4=1.8 mm, L_1=800.0 mm, L_2=300.0 mm, and L_3=15.0 mm.

2.2 Governing equations

The governing equations consist of:

Mass conservation:
$$\frac{\partial \rho}{\partial t} + \rho \frac{\partial u_i}{\partial x_i} = 0 \tag{1}$$

Momentum conservation:
$$\rho \frac{\partial (u_j)}{\partial t} + \rho \frac{\partial (u_i u_j)}{\partial x_i} = -\frac{\partial p}{\partial x_j} + \frac{\partial}{\partial x_i}(\tau_{ij} - \overline{\rho u_i' u_j'}) \tag{2}$$

Species continuity:
$$\frac{\partial (X_n)}{\partial t} + \rho \frac{\partial (u_i X_n)}{\partial x_i} = -\frac{\partial}{\partial x_i} J_n + \dot{\omega}_k \tag{3}$$

Energy conservation:
$$\frac{\partial (\rho h)}{\partial t} + \frac{\partial (\rho u_i h)}{\partial x_i} = \frac{dp}{dt} + \frac{\partial}{\partial x_i}\left[(\lambda + \lambda_t)\frac{\partial T}{\partial x_i}\right] - \sum_{n=1}^{N} \frac{\partial}{\partial x_i} h_n J_n + \frac{\partial (u \tau_{ij})}{\partial x_i} + \dot{Q} \tag{4}$$

where, p is instantaneous pressure, τ_{ij} is viscous stress, t denotes time. ρ, u_i are density, and velocity in x_i direction respectively. h is the enthalpy of the mixture, X_n, J_n and h_n are the mass fraction, diffusion flux and enthalpy of the species"n" and $\dot{\omega}_k$ is the species source term due to chemical combustion. T is temperature, λ is thermal conductivity and $\dot{Q}$ is the heat source term due to combustion. A standard $k-\omega$ model is selected in the present simulations. The turbulence model was validated and applied in previous literature [47-49], since it is more robust to simulate low Reynolds number flows [50, 51]. The chemical reaction mechanism of either hydrogen- or propane-fueled combustion is assumed to be a one-step reaction as:

$$2H_2 + (O_2 + 3.76N_2) \rightarrow 2H_2O + 3.76N_2 \tag{5a}$$

$$C_3H_8 + 5(O_2 + 3.76N_2) \rightarrow 3CO_2 + 4H_2O + 18.8N_2 \tag{5b}$$

In our model, a turbulence-chemistry interaction model is set to be the eddy-dissipation (ED) model. The net rate of production of species n due to chemical reaction r is given as:

$$R_{n,r} = \min\left(Av'_{n,r}M_{w,n}\rho\frac{\varepsilon}{\kappa}min\left(\frac{Y_R}{v'_{R,r}M_{w,R}}\right), ABv'_{n,r}M_{w,n}\rho\frac{\varepsilon}{\kappa}\frac{\sum_P Y_P}{\sum_m^N v''_{m,r}M_{w,m}}\right) \quad (6)$$

where A =4.0 and B=0.5, $v'_{n,r}$ is the stoichiometric coefficients of reactants and $v''_{n,r}$ represents those of chemical products. ρ and M_w are density and the molecular weight. ε/k represents the turbulent mixing time scale. In the $k-\omega$ model, turbulence time scale can be calculated by $= \beta^*\omega$, where usually β^*= 0.09 [52, 53]. Subscripts R and P represent the reactants and products respectively. It can be seen from Eq. (6) that the final chemical reaction rate is determined by the minimum value of the source term on the right-hand-side.

2.3 Entropy generation analysis

The volumetric entropy generation rates are calculated by:

$$S_{total} = \frac{\tau\cdot\nabla\mathbb{V}}{T} + \frac{\lambda\nabla T\cdot\nabla T}{T^2} + R_0\sum_n\frac{\rho D_{n-mix}}{X_n}\nabla Y_n\cdot\nabla X_n - \sum_n\frac{\mu_n R_n}{T} \quad (7)$$

Eq. (7) shows the volumetric entropy generation rates by various irreversible processes. The first term on the right-hand side of Eq. (7) is related to the fluid flow friction (S_{vis}). The second term is due to the effect of energy flux, in which only the effect of heat conduction is considered (S_{cond}). Then the third term describes the mass diffusion contribution (S_{diff}). In addition, the chemical reaction on entropy generation rate is represented by the last term (S_{chem}).

The detailed expressions of these four contributions to the entropy generation are given as:

$$S'_{vis} = \frac{\mu}{T}\left[2\left\{\left(\frac{\partial v}{\partial x}\right)^2 + \left(\frac{v}{x}\right)^2 + \left(\frac{\partial v}{\partial y}\right)^2\right\} + \left(\frac{\partial u}{\partial y} + \frac{\partial v}{\partial x}\right)^2 - \frac{2}{3}\left(\frac{1}{x}\frac{\partial(x\cdot u)}{\partial x} + \frac{\partial v}{\partial y}\right)^2\right. \quad (8)$$

$$S'_{cond} = \frac{\lambda}{T^2}\left[\left(\frac{\partial T}{\partial x}\right)^2 + \left(\frac{\partial T}{\partial y}\right)^2\right] \tag{9}$$

$$S'_{diff} = R_0\rho\frac{D_{n-mix}}{X_n}\left[\frac{\partial Y_n}{\partial x}\frac{\partial X_n}{\partial x} + \frac{\partial Y_n}{\partial y}\frac{\partial X_n}{\partial y}\right] \tag{10}$$

$$S'_{chem} = -\sum_n \frac{\mu_n\omega_n}{T} \tag{11}$$

In Eqs. (8) - (11), μ is viscosity. u and v are flow velocity in the x and y directions, ρ is the density and λ is the effective thermal diffusivity. Y_n , X_n , D_{n-mix}, ω_n ,μ_n and are the mass fraction, mole fraction, diffusion coefficient, reaction rate and the chemical potential of the species n respectively. $R_0$is the gas constant (8.314 J/mol·K). For an ideal gas mixture, μ_n is given as

$$\mu_n = \bar{h}_n^0(T) - T\cdot\bar{s}_n^0(T) + R_0 T ln(\frac{Y_n P}{P_{ref}}) \tag{12}$$

Where P_{ref}= 101325.0 Pa. $\bar{h}_n^0(T)$ and $\bar{s}_n^0(T)$ is the reference enthalpy and entropy at $P_{ref}$of the species "n".

It has been confirmed in previous studies [54, 55] that the contribution of the viscous process on the entropy generation is relatively low. Thus, the entropy generation due to the viscous effect is assumed negligible in this work. The total entropy generation rate can be then approximated as:

$$S_{total} \approx S_{cond} + S_{diff} + S_{chem} = \iiint \left(S'_{cond} + S'_{diff} + S'_{chem}\right)dV \tag{13}$$

The second law efficiency η_{II} can be written as:

$$\eta_{II} = 1 - \frac{T_0\cdot S}{Q} \tag{14}$$

where T_0 is the ambient temperature (T_0 = 300K) and Q is the heat release rate of the combustor.

2.4 Boundary Conditions

The velocity fluctuation excited by acoustic waves is generated by User Defined Function (UDF). The unsteady velocity is described as:

$$u_y(t) = |\bar{u}|\left[1 + \left|\frac{u'}{\bar{u}}\right| \cdot \sin(\omega t + \theta_0)\right] \quad (15)$$

where $u_y(t)$ is the velocity in axial direction, $\bar{u}$ is the flow mean velocity at the bottom inlet of the combustor. u' represents the fluctuating velocity, ω and t are angular frequency and time. θ_0 is the initial phase. In our studies, the initial phase is set as θ_0=0 rad， the mean flow velocity is set as $\bar{u}$= 0.15 m/s. The flow perturbation intensity is set as $|u'/\bar{u}|$ = 20% or 10%. Gaseous hydrogen (H_2) is supplied as the fuel in the current modelled combustor. To obtain the same heat release in combustor with the experimental tests, the hydrogen injection velocity is 2.4 m/s. The top outlet boundary is set as a pressure outlet. The boundary condition of sidewalls of the modelled combustor is set as no-slip, adiabatic and no chemical reaction.

3. Validation of numerical model

3.1 Mesh- and time-independence study

For completeness, mesh- and time-independent studies are conducted first. Three different number of meshes are generated by Ansys workbench meshing (V18.2). The axial velocity at 40mm above the nozzle (y = 440mm) is recorded and compared along the centerline of the tube. Fig.2 (a) shows the axial velocity u(t), as the three meshes are applied. It can be seen that there is a negligible difference of the predicted velocities between the medium and fine meshes. The coarse mesh leads to a slightly larger-amplitude velocity fluctuation. Thus the medium mesh with 20580 cells is selected for the following simulations. Fig. 2(b) shows the time-independent study results, as the time step is set to Δt =0.0002 s, 0.0001 s, and 0.00005 s. It can be seen that there is little difference of the recorded axial velocity between the time steps of 0.0001 s and 0.00005 s. Thus

the time step Δt =0.0001 s is chosen in the current studies to save computing time, whilst achieving an acceptable accuracy.

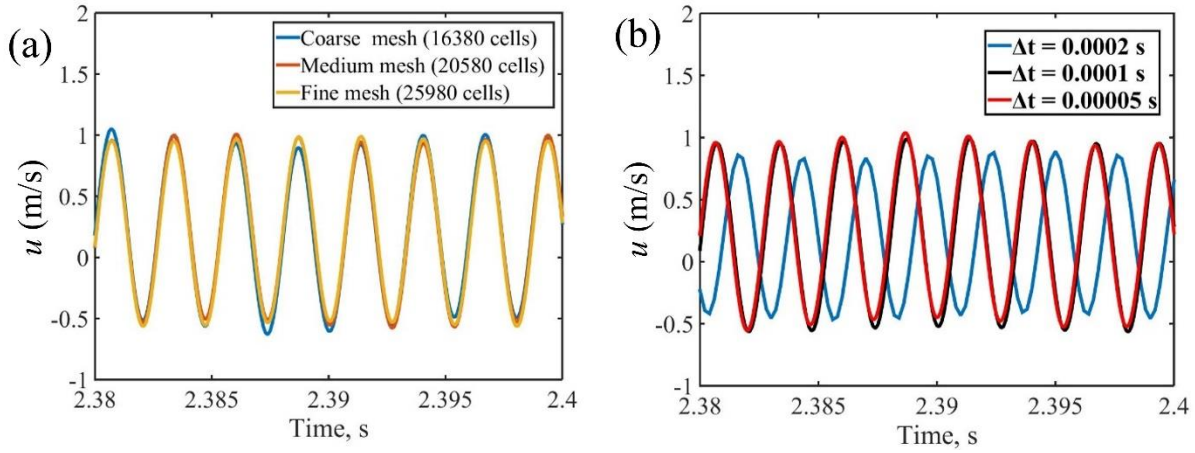

Fig. 2. (a) Variation of the axial velocity with time, as the number of the meshes is set to 3 different values, (b) variation of the axial velocity with time, as the time step is set to 3 different values.

3.2 Validation of Numerical Model

With the mesh- and time independent studies completed, the numerical model needs to be validated, before it is used to study the flame-acoustics interaction in the longitudinal tube with a loudspeaker implemented. Note that the simulations are conducted in a time domain by applying acoustic disturbances consisting of a single frequency at a time. The interested frequency range is between 40 and 600 Hz where incremental frequency step is set to 5 Hz. Fig. 3(a) shows the normalized pressure fluctuation varying with frequency. Comparison is made between the numerical and the experimental results [25, 26]. It can be seen that there are four resonant frequencies: 65 Hz, 220Hz, 385 Hz and 525Hz over the interested frequency range. These frequencies are in good agreement with the experiment measurements by Chen et al. [25]. In addition, their experimental measurements on the turbulence intensities via applying PIV are compared with the present numerical simulations. This is shown in fig. 4. Here three different

frequencies, i.e. 90, 150 and 200Hz are considered with the fuel injector placed at y= 400 mm. It can be seen that the feature of turbulence intensities in the tube calculated by simulation have the same trend of experiment results as frequencies varying.

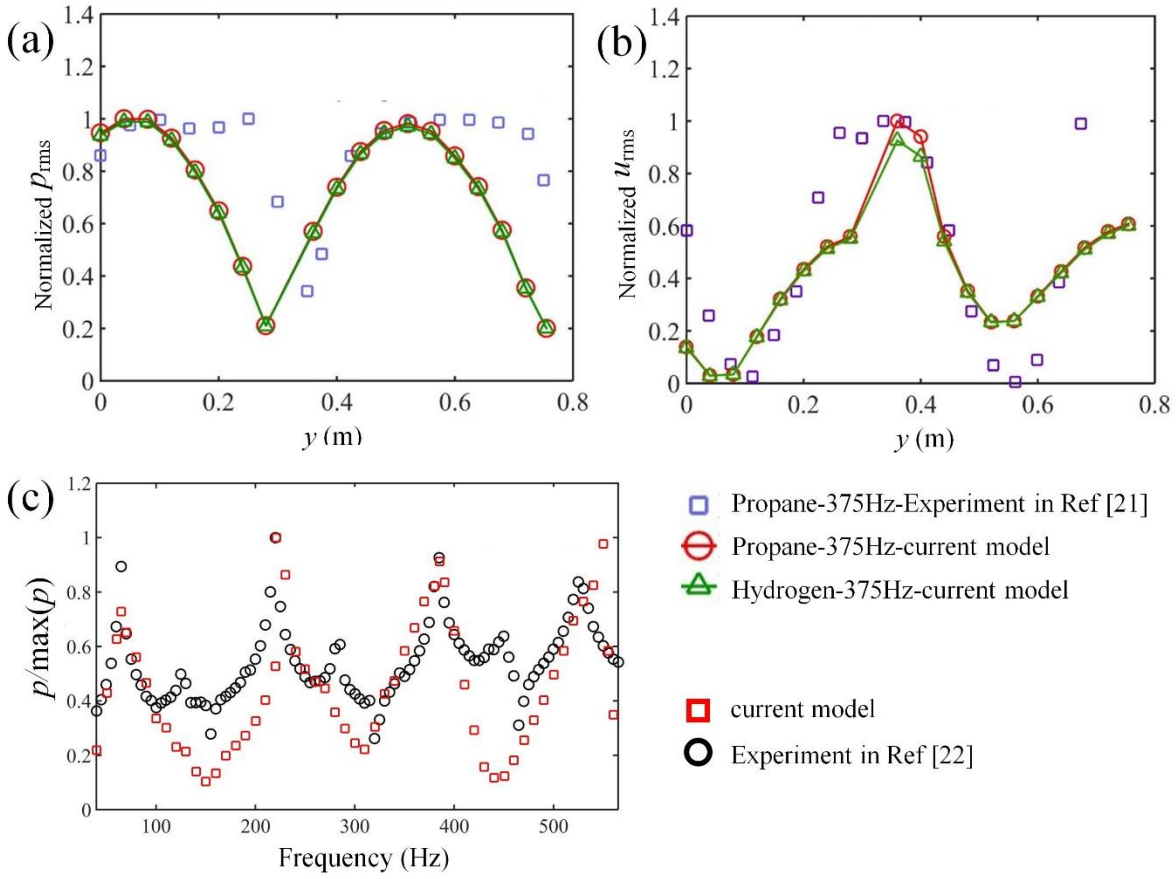

Fig. 3 Validation with the experimentally measured mode shape in terms of (a) Normalized prms (b) Normalized urms [24], (c) the resonance frequencies [25].Here the root mean square values of pressure and velocity are defined as:

$$p_{rms} = \sqrt{\frac{1}{N}\sum_N (p(i))^2}, \quad u_{rms} = \sqrt{\frac{1}{N}\sum_N (u(i))^2}.$$

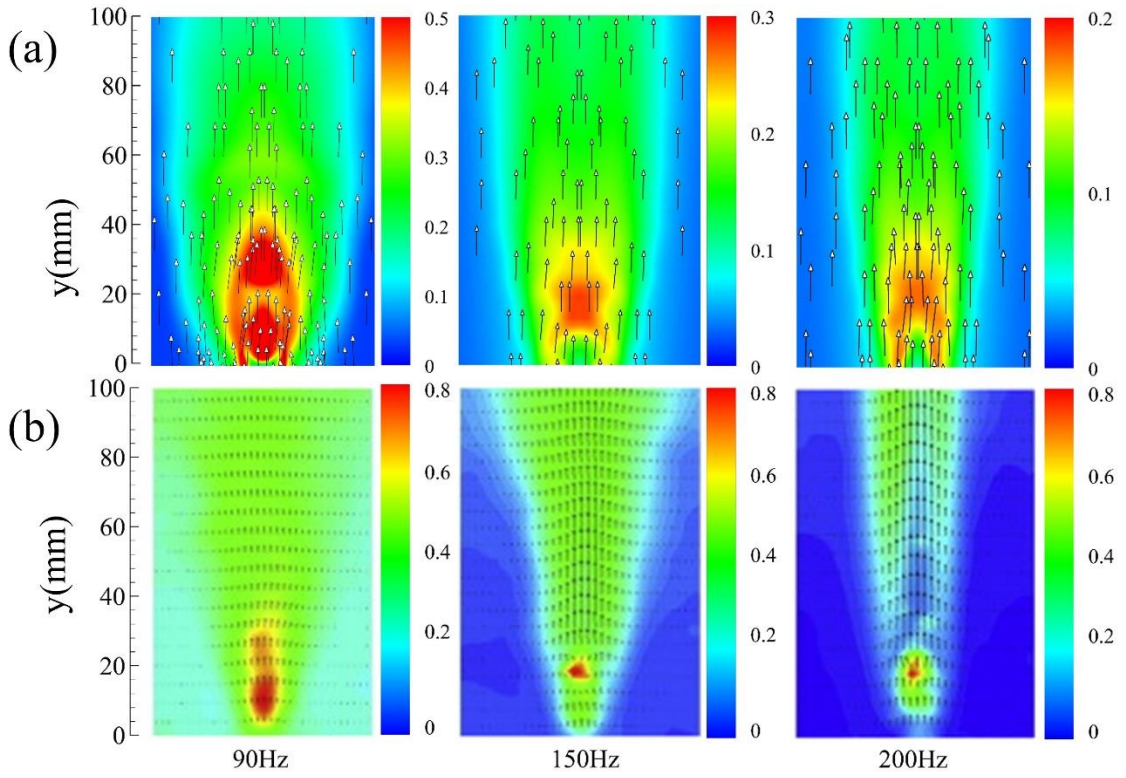

Fig. 4. Validation with the experimental results: turbulence intensities: (a) CFD results (b) Experiment results, as the propane is injected with a velocity of 0.32m/s. [25]

Further validation is conducted by modifying the model and comparing with the experimental measurements obtained by Farhat et al. [24]. In their experiment, the fuel nozzle is centrally placed at y= 330 mm. Propane is supplied as fuel and the mass flow rate is 80 ml/min which corresponds to an injecting velocity of 0.52m/s. In addition, experimentally measured mode shapes are illustrated in Fig. 3(b) and (c) respectively in terms of pressure and velocity RMS values which are normalized with their maximum values for a clear comparison. Fig. 5 shows the comparison of the measured flame behaviors and shapes with the predicted ones, as the flame is placed at different axial locations but the same acoustic disturbances (375 Hz and 10 volts) are applied. The node and antinode of mode shape has been successfully predicted in the numerical results. The

flames in the experiments are obtained by using an intensified CCD camera (Lavision) and the simulation flames are presented as contours of temperature. It is clear that the flame behavior and shape depends on the nozzle position. In addition, the flame structures, shapes and colors are consistent between the numerical predictions and the experimental measurements, no matter whatever the supplied fuel is propane or hydrogen. When hydrogen is applied, the flame has a low-temperature inner core due to the high-speed low-density hydrogen injection. This is fundamentally different from the propane-fueled flame. In the experiments, there is a lift-off distance for the jet diffusion flames, but this feature does not occur in simulation, probably caused by the simplified combustion model and chemical reaction. Apart from the lift-off distance, the general features of the jet diffusion flame predicted by our numerical simulations match well with the ones observed in experiments.

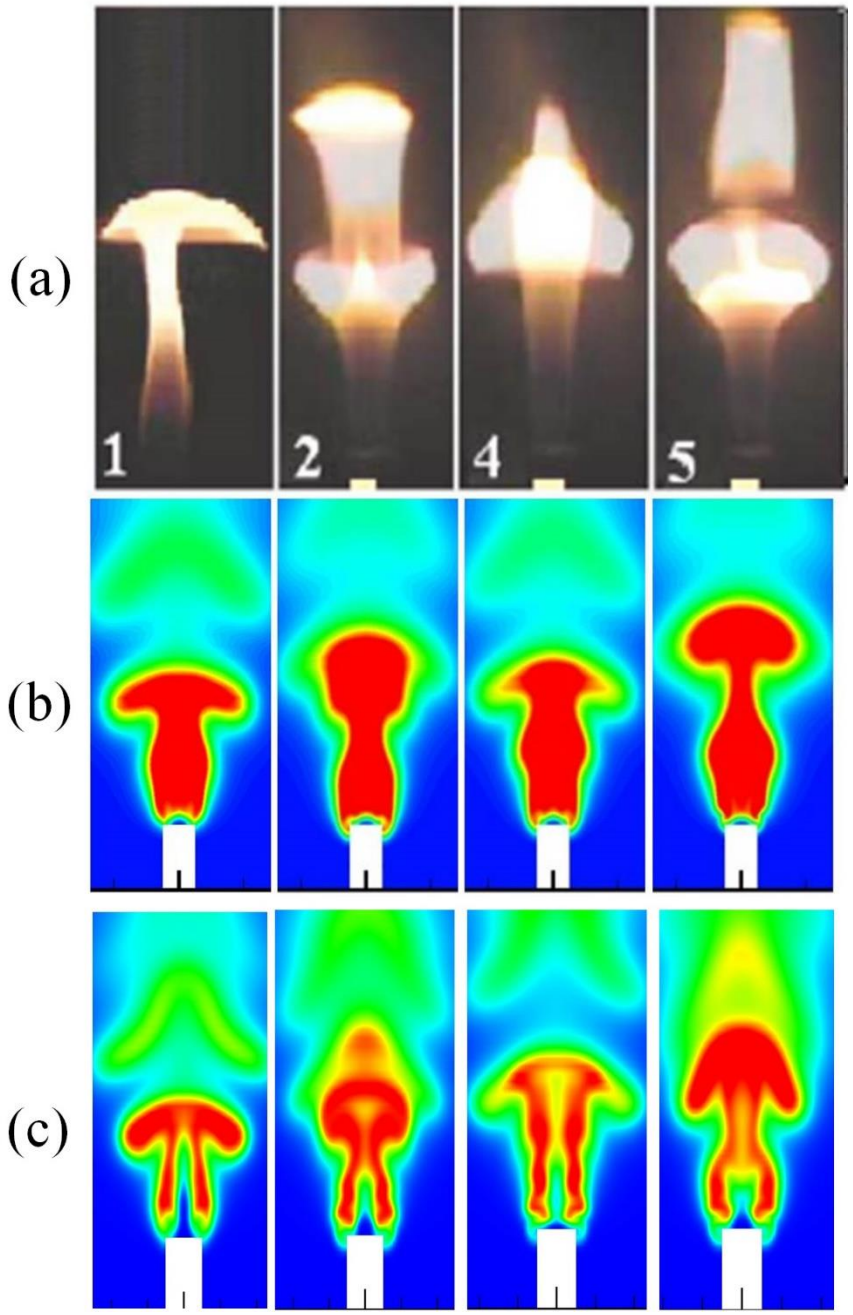

Fig. 5. Comparison of the experimentally measured flame with the numerically predicted one (a) experimental propane flame [24] (b) numerical propane flame (c) numerical hydrogen flame, as the fuel nozzle is placed at 4 different axial locations.

4. Results and Discussion

4.1 Entropy generation and thermodynamic second law efficiency

4.1.1 Effects of fuel

The effect of different fuels, i.e. H_2 and C_3H_8 on entropy generation is compared by placing the nozzle at y = 400 mm and the acoustic forcing frequency is set as 385Hz. In order to keep the heat release rates of both hydrogen and propane the same in the combustor, propane is injected with a velocity of 0.32m/s and hydrogen is injected with a velocity of 2.4 m/s. Fig.6 (a) and (b) illustrate the entropy generation of the hydrogen- and propane-fueled diffusion flame respectively. It can be seen that the hydrogen-produced entropy contours involves a continuous wave pattern propagating upwards. However, a mushroom-like contour is observed on the propane-fueled flame. In addition, less toroidal vortices around the nozzle are seen on the propane flame in comparison with the hydrogen-fueled one. This is most likely due to the lower inject velocity. Finally, the entropy generation from either hydrogen- or propane-fueled flames are periodically evolved. Table.1 shows the volumetric entropy generation rate (S) and the second thermodynamic law efficiency (η_{II}), as C_3H_8 and H_2 are fueled. It can be seen that the dominant contribution of entropy generation depends on the heat conduction process, while the diffusion process contributes the minimum, no matter the fuel is hydrogen or propane. When propane is burnt, S_{total} is less than that of hydrogen. However, η_{II} is higher.

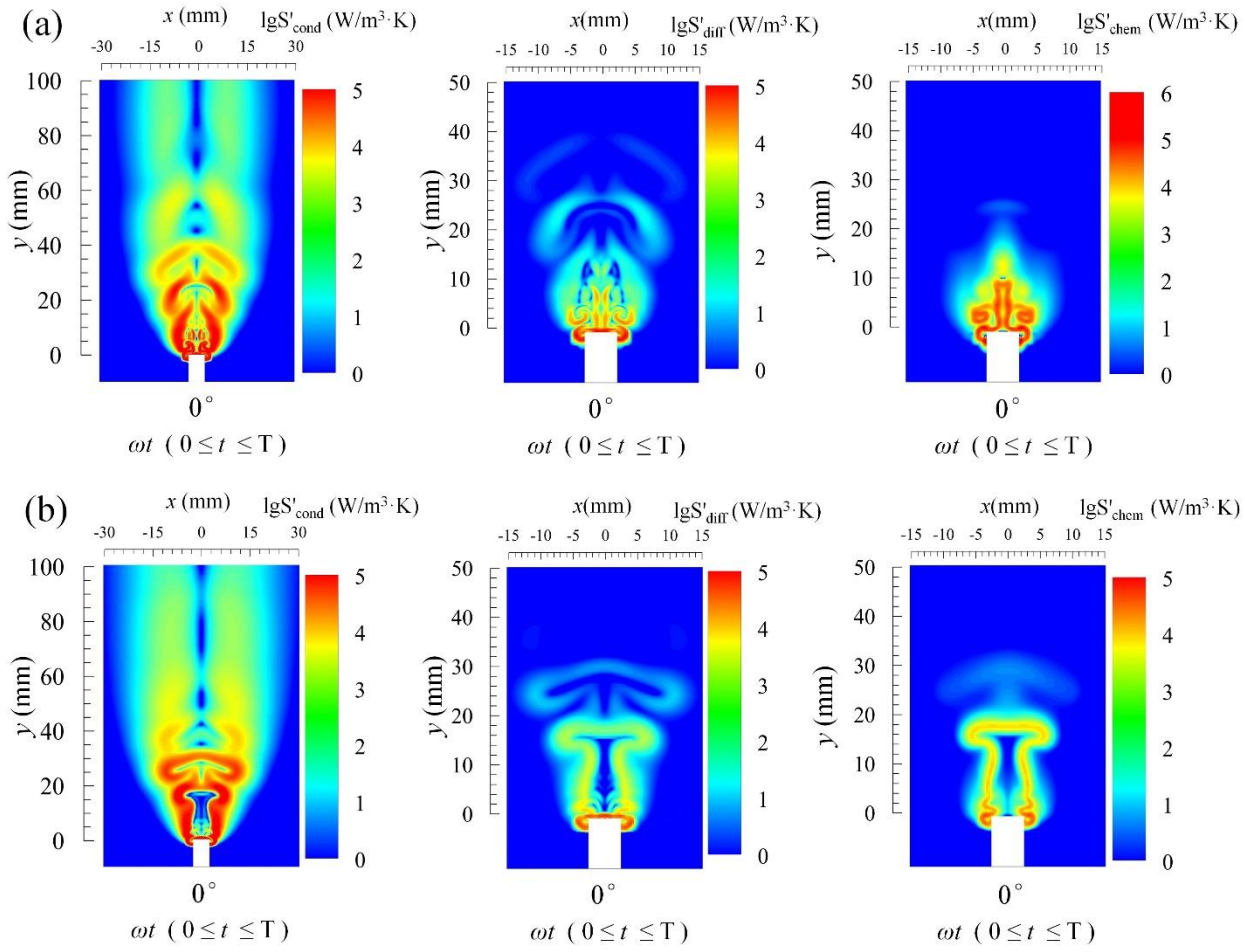

Fig. 6. Contour comparison of entropy generation as (a) H_2 is fueled (b) C_3H_8 is fueled, and $\bar{u} = 0.15\ m/s, u'/\bar{u} = 20\%, \omega\ /\ 2\pi = 385Hz$.

Table 1. Comparison of volumetric entropy generation rate (S) and the second law efficiency (η_{II}) , as propane and hydrogen are fueled.

Types of fuel	S_{cond}/S_{total}	S_{diff}/S_{total}	S_{chem}/S_{total}	S_{total}(W/K)	η_{II} (%)
Hydrogen(H_2)	80.3%	2.7%	17%	0.02894	83.68
Propane(C_3H_8)	95.4%	1.9%	2.7%	0.02666	88.27

4.1.2 Effects of acoustic frequency and amplitude

The effect of acoustic perturbations on entropy generation is examined by placing the nozzle at y = 400 mm and the acoustic forcing frequency is set to 90Hz, 200Hz and 385Hz. These frequencies selections are consistent with the experimental measurements in Refs. [25， 26]. Before the entropy generation is examined resulting from 1) heat conduction, 2) mass diffusion and 3) chemical reaction, it would be interesting to reveal the periodic changes of the acoustic fluctuation imposing on the hydrogen-fueled flame. Fig.7 shows the variation of the axial velocity at 40 mm above the fuel injector with phase ωt under three different frequencies excitation. It can be seen that 385Hz acoustic fluctuations are associated with the maximum amplitude axial velocity perturbations. The 200 Hz acoustic disturbances lead to a minimum axial velocity fluctuation.

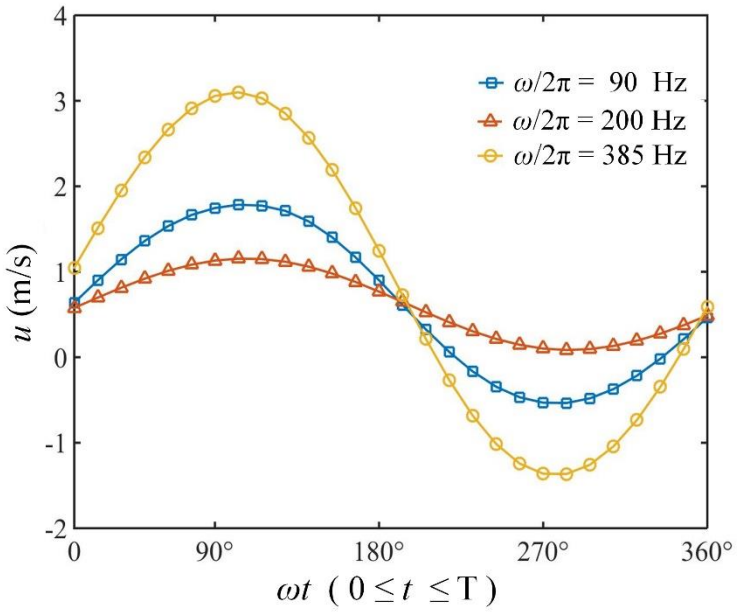

Fig. 7. Variation of the axial velocity at 40 mm above the fuel injector over an acoustic period.

Eq. (9) reveals that effective thermal conductivity and temperature gradient are two important influencing factors on entropy generation. This could be described as heat conduction entropy

denoted by S'_{cond}. Fig.8 shows the S_{cond} distributions in the combustor with the excitation frequency within an acoustic period. When the acoustic frequency is 200 Hz, the distribution of entropy generation is conical shape and high entropy generation area stay at the two sides of downstream of nozzle where the combustion takes place in jet diffusion flame. The distribution region almost have no change in a period. Wave shape can be found at the distribution of volumetric entropy generation at 90Hz, which because the velocity disturbance increases. The velocity perturbation is highest under the excitation of 385Hz. Under the excitation of 385Hz, the height of entropy generation rate is shorter, mushroom-like appearance can be seen and the distribution region of entropy generation move up and down in a period. The peak value of entropy generation rate at the excitation frequency of 385 Hz can reach 2.077×10^6 W/m^3·K which is higher than 2.943×10^4 W/m^3·K at 90 Hz and 2.788×10^4 W/m^3·K at 200Hz. The integration of volumetric entropy generation induced by thermal conduction has the same trend, which can be seen at Fig. 11(a). Integration of heat conduction entropy S_{cond} at 385Hz is 0.02324 W/K, which is higher than at other two frequencies, 0.0181 W/k at 90Hz and 0.01781 W/k at 200Hz. This is because the flame surface area increases under the high velocity disturbance, which can enhance the heat transfer.

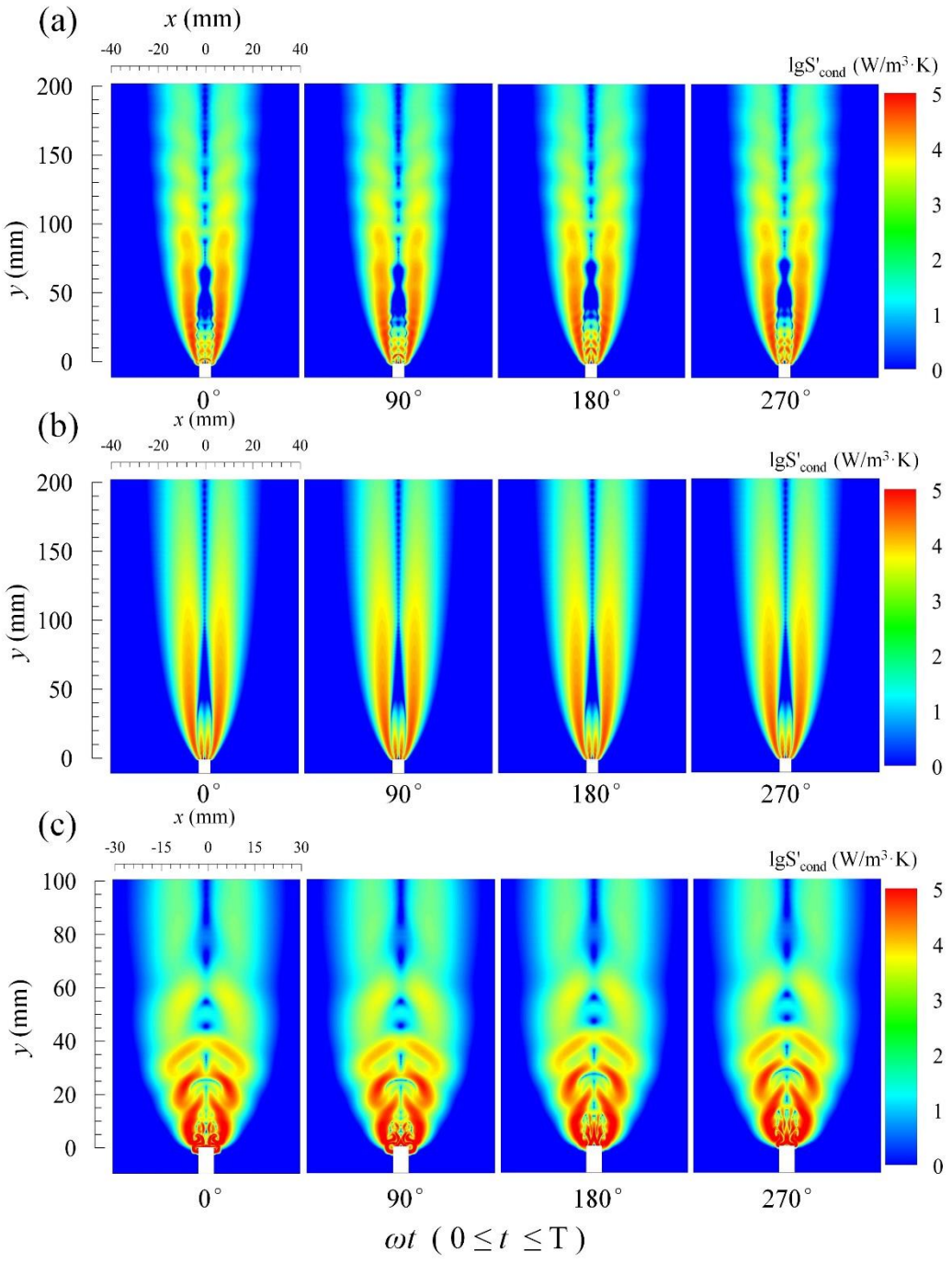

Fig. 8. Contour comparison of volumetric entropy generation resulting from heat conduction S_{cond} over an acoustic period: (a) $\omega/2\pi = 90$Hz (b) $\omega/2\pi = 200$Hz (c) $\omega/2\pi = 385$Hz, as $\bar{u} = 0.15\ m/s$, and $u'/\bar{u} = 20\%$.

It has been shown in Eq. (11) that the volumetric entropy generation could result from mass diffusion. This is classified as mass diffusion entropy denoted by S'_{diff}. It depends on the gradient of mass fraction and mole fraction. Fig.9 depicts the S'_{diff}distributions in the combustor with the excitation frequency within a period of oscillation. As depicted in Fig.9, the area of high entropy generation decreases with the increasing distance from nozzle because the chemical rate of diffusion combustion is fast near the nozzle outlet position. As the disturbance increase, wave shape can be seen at 90Hz and toroidal vortices are observed at 385Hz. The distribution region of volumetric entropy generation at 385 Hz is quite short. This is because the strong velocity disturbance make the reaction fiercer and faster. The peak value of mass diffusion entropy generation at the excitation frequency of 385 Hz can reach 2.533×10^{6} W/m^3·K which is higher than 7.173×10^{4} W/m^3·K at 90 Hz and 1.021×10^{5} W/m^3·K at 200Hz. The integration of mass diffusion entropy generation S_{diff} is shown at Fig. 11(a). Integration of mass diffusion entropy at 385Hz is 7.89239×10^{-4} W/K that is lower than at other two frequencies, 0.00142W/K at 90Hz and 0.00153W/k at 200Hz. This is because the high reversal velocity make the diffusion of fuel slow.

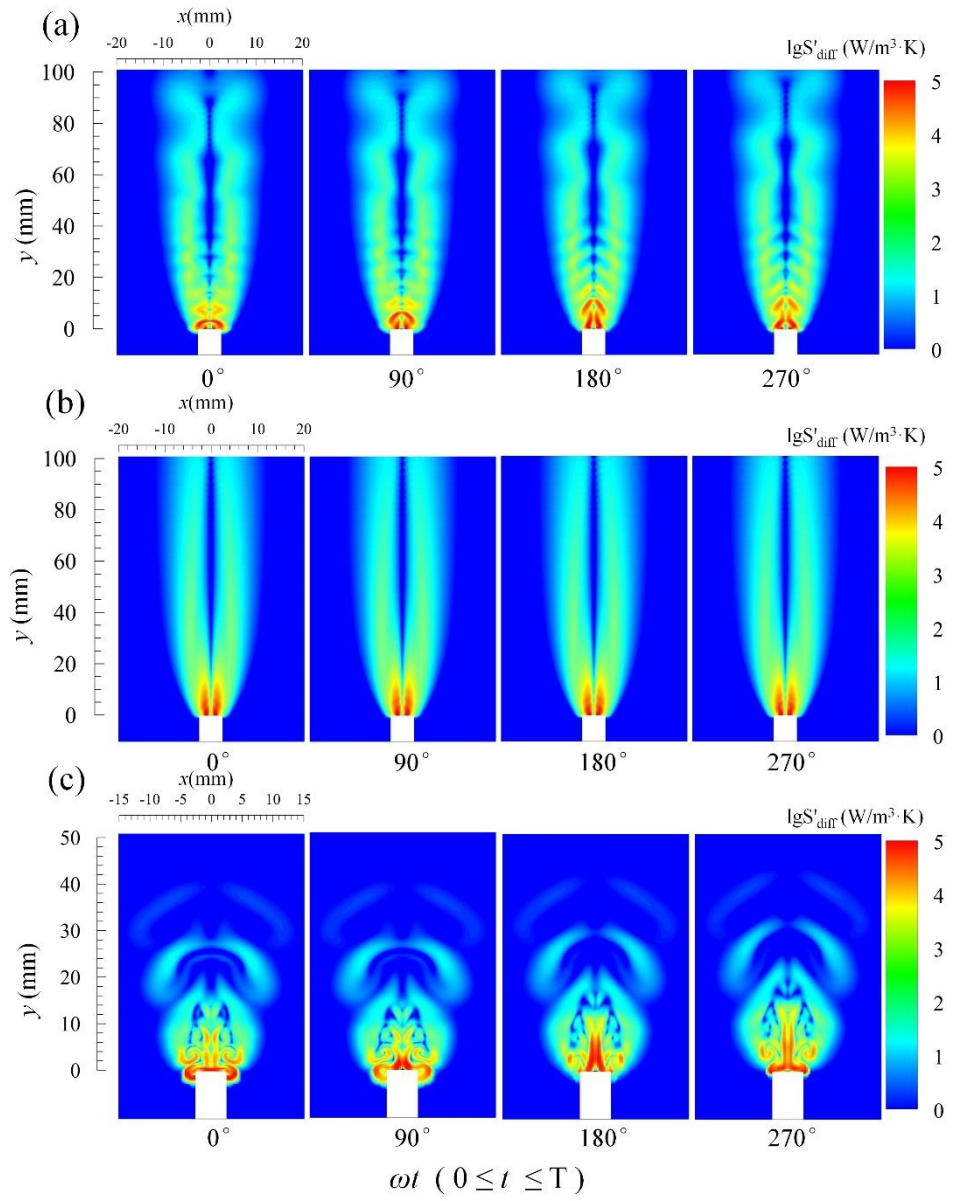

Fig. 9. Contour comparison of volumetric entropy generation resulting from mass diffusion S_{diff} over an acoustic period: (a) $\omega/2\pi = 90$Hz (b) $\omega/2\pi = 200$Hz (c) $\omega/2\pi = 385$Hz, as $\bar{u} = 0.15\ m/s$, and $u'/\bar{u} = 20\%$.

Fig.10 illustrates the entropy generation due to the chemical reaction S'_{chem}over an acoustic period. It can been seen from the distribution of entropy generation due to chemical reaction that

the high entropy generation region locates at the flame edge area. This is because the chemical reaction in the diffusion flame mainly occurs in the maximum temperature region [39]. When the acoustic frequency is set to 200Hz, the distribution shape is conical and stable ove a period. Wave shape can be found at the distribution of volumetric entropy generation and necking was found to occur at the tip at 90Hz. Under the excitation of 385Hz, the distribution of entropy move up and down and toroidal vortices occur. The peak value of entropy generation caused by chemical reaction at the excitation frequency of 385 Hz can reach 5.053×10^{5} W/m^{3}·K, which is higher than at 90 Hz 1.147×10^{4} W/m^{3}·K and at 200Hz 9.723×10^{3} W/m^{3}·K. The integration of entropy due to chemical reaction S_{chem} is shown Fig. 11(a). Integration of chemical reaction entropy S_{diff} at 385Hz is 4.915×10^{-3} W/K which is higher than at other two frequencies, at 90Hz 3.648×10^{-3} W/K and W/K at 200Hz 3.576×10^{-3}. This is because the high velocity causing the combustion instability phenomenon.

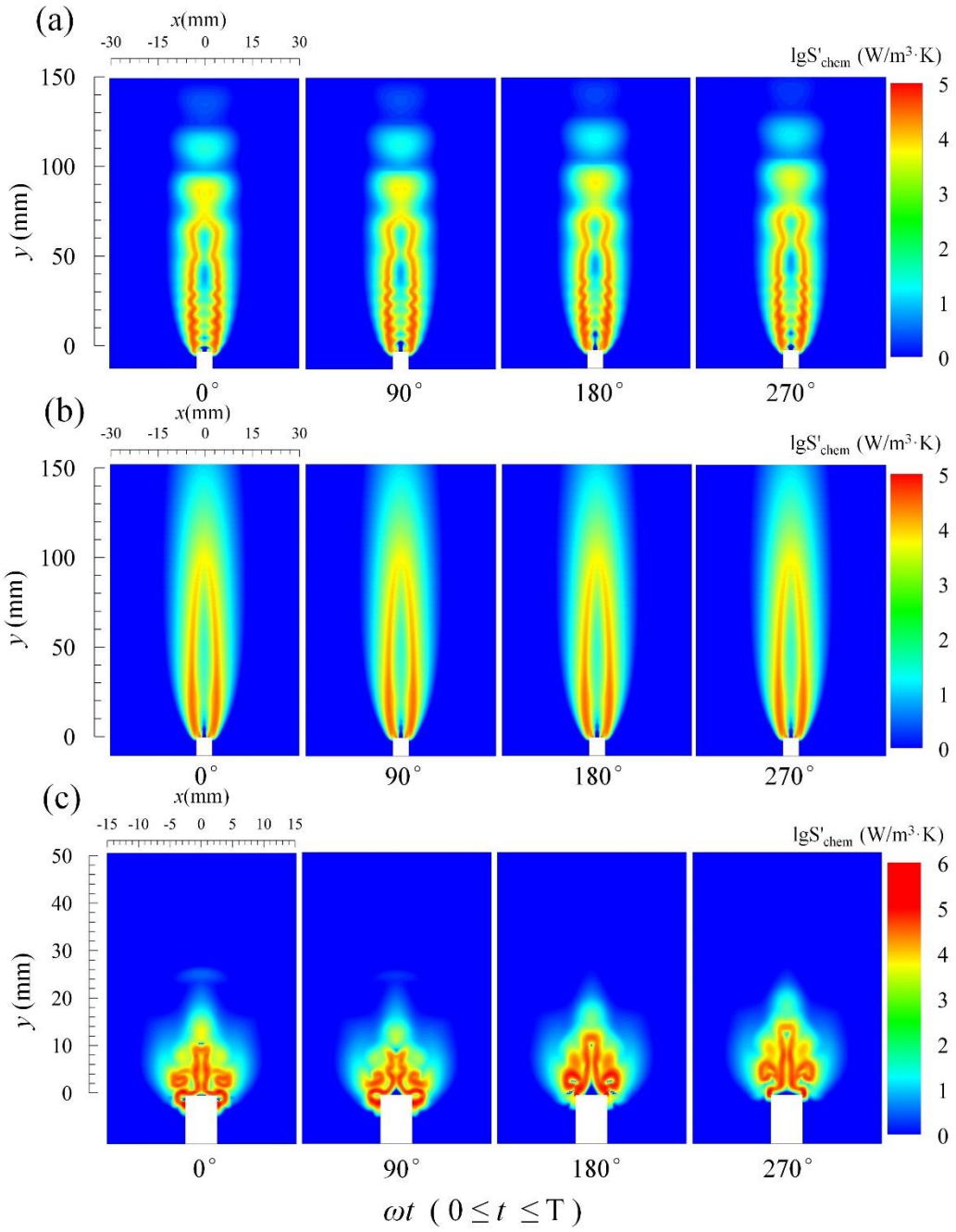

Fig. 10. Contour comparison of volumetric entropy generation resulting from chemical reaction S_{chem} over an acoustic period: (a) $\omega/2\pi = 90$Hz (b) $\omega/2\pi = 200$Hz (c) $\omega/2\pi = 385$Hz as $\bar{u} = 0.15\ m/s$, and $u'/\bar{u} = 20\%$.

Fig.11 (a) and (b) show integrated entropy generation rates and entropy generation induced by three effects at three frequencies. It is found that, among three physical processes, thermal conduction is playing a dominant role on total entropy generation, while mass diffusion contributes the lowest. With the acoustic excitation at 385Hz, the total entropy generation is maximized and the second law efficiency is minimized.

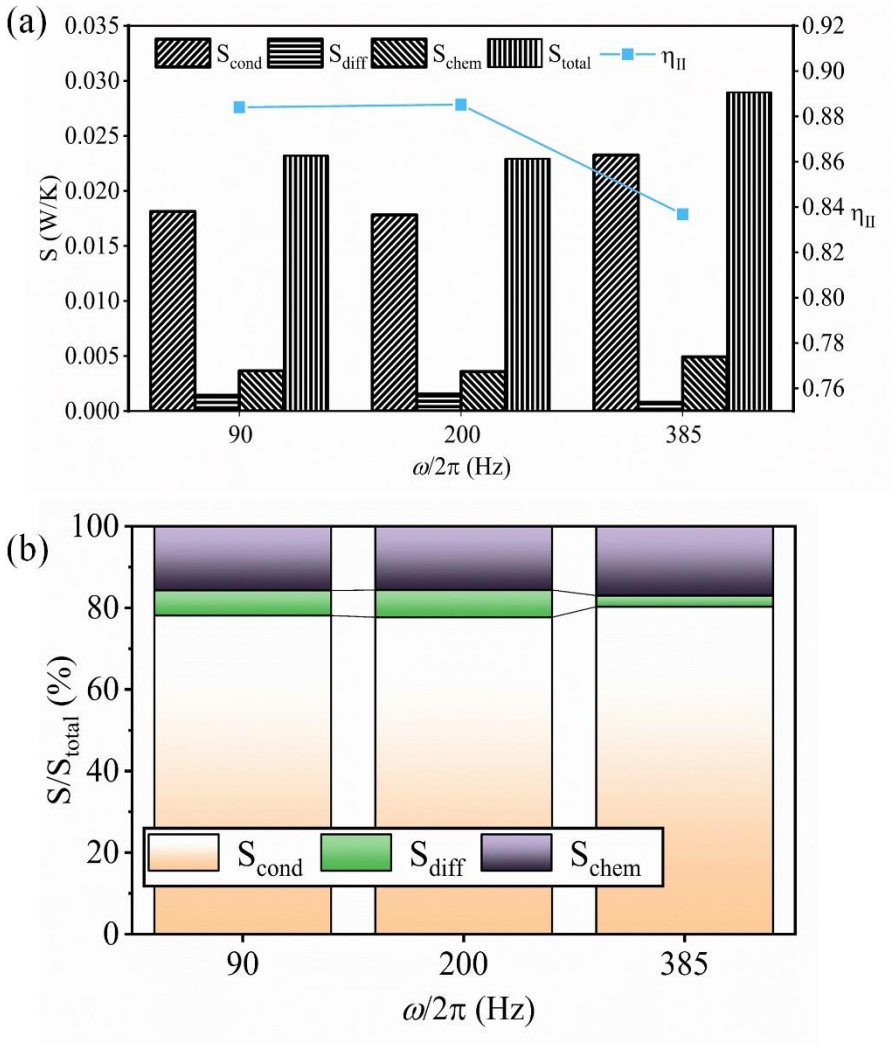

Fig. 11 Comparison of (a) volumetric entropy generation rate (S) and the second law efficiency (η_{II}) , (b) entropy generation contribution, as acoustic frequency is set to 3 different values

Table.2 illustrates the effect of acoustic amplitude on the entropy generation. Two different ratios $|u'/\bar{u}| = 20\%$ and $|u'/\bar{u}| = 10\%$ are selected. It is clear that the contribution due to the S_{chem} remains almost unchanged. However, S_{cond} and S_{total} are increased slightly with increased $|u'/\bar{u}|$. η_{II} and S_{diff} is decreased with more intensified acoustic disturbances, illustrating that increased amplitude improves heat transfer but slows down the diffusion of hydrogen due to higher reversal velocities.

Table 2. Volumetric entropy generation rate (S) and the second law efficiency (η_{II}), as the acoustic disturbances are set to two different amplitudes

Amplitude	S_{cond}/ S_{total}	S_{diff}/S_{total}	S_{chem}/ S_{total}	S_{total}(W/K)	η_{II} (%)
$\|u'/\bar{u}\| = 20\%$	80.3%	2.7%	17%	0.02894	83.68
$\|u'/\bar{u}\| = 10\%$	79.1%	3.9%	17%	0.02524	87.34

4.1.2 Effects of the nozzle axial location

The nozzle axial location effect on entropy generation is evaluated the acoustic frequency is chosen 385 Hz, which corresponds to the 3rd resonant frequency. As shown in Fig. 12, the mode shape has two velocity nodes along the combustion tube. The effect of fuel nozzle location is evaluated, being placed at 3 different locations, y=120 mm, 400 mm and 550 mm. The location of y=120 mm and 550 mm are quite close to the velocity nodes, whilst y=400 mm is near the velocity anti-node.

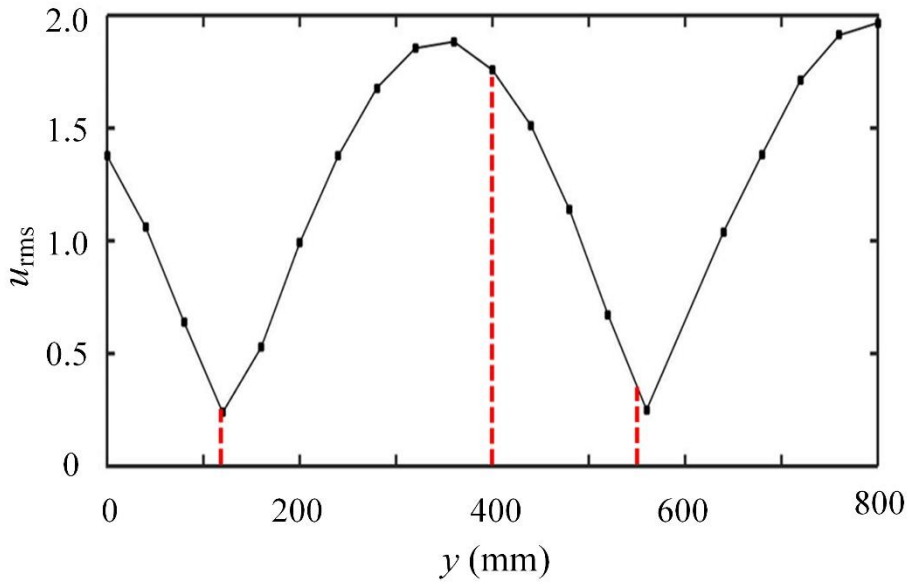

Fig. 12. Predicted mode shape in terms of u_{rms} in axial direction, as the acoustic disturbances at 385Hz are applied.

Fig.13 shows the volumetric entropy generation resulting from heat conduction, as the nozzle is placed at these 3 different nozzle positions. It can be seen that at y=120 and 550 mm, a steady V-shaped entropy contour is produced. This is most likely due to the acoustics-induced stagnation effect. Over the acoustic period, there is almost no change in terms of the entropy contours. However, when the nozzle is placed at y=400 mm, a spatially wavy entropy contour is observed and the entropy generation is greatly increased. In addition, the entropy contour near the nozzle outlet is found to change dramatically over the acoustic period. This is quite different from what happened when the nozzle is placed at velocity node locations i.e. y=120 and 550 mm.

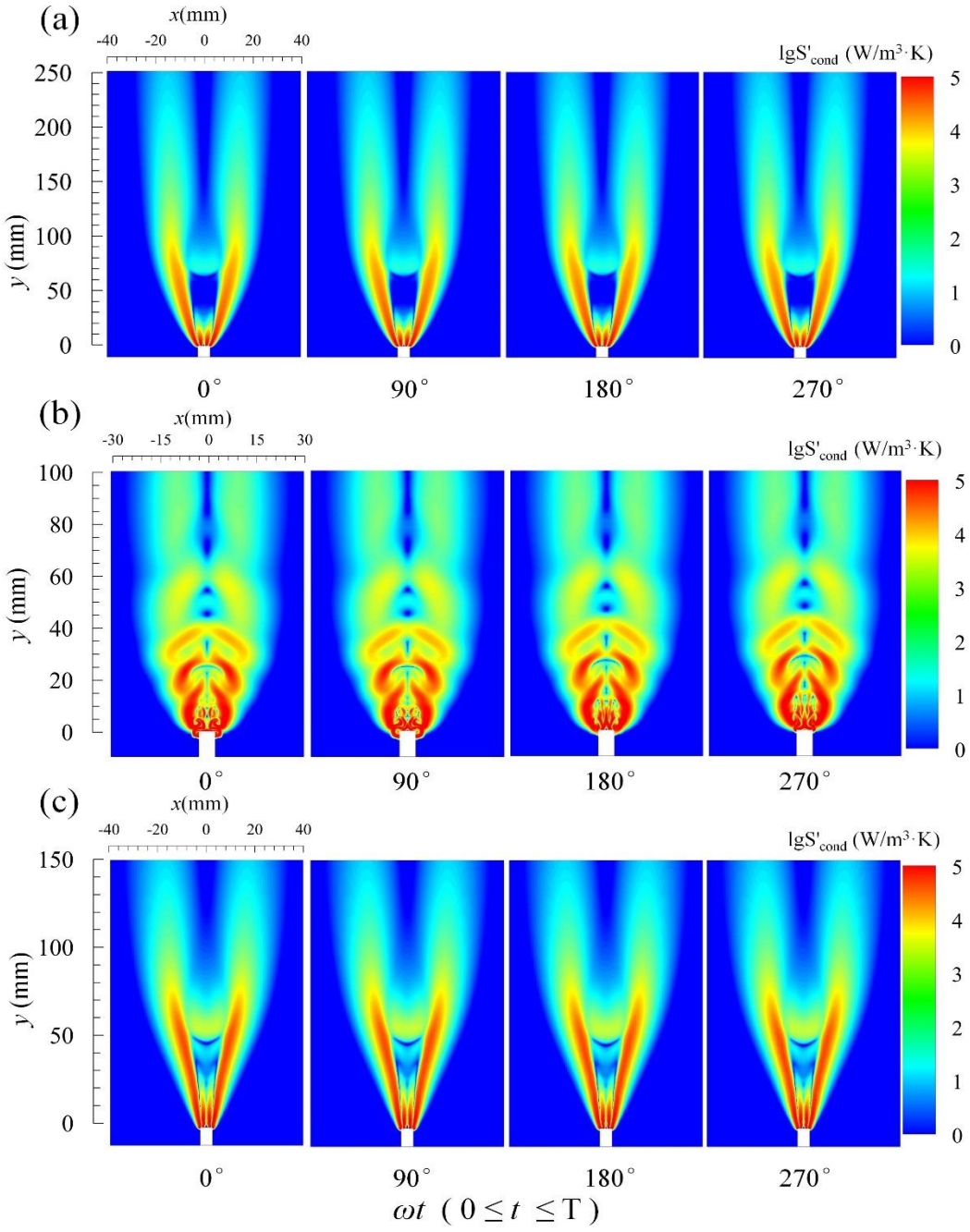

Fig. 13. Contour comparison of volumetric entropy generation resulting from heat conduction S_{cond} over an acoustic period: nozzle is placed at (a) y=120mm (b) y=400mm (c) y=550mm, as $\bar{u} = 0.15\ m/s$, $u'/\bar{u} = 20\%$, and $\omega/2\pi = 385$Hz.

Fig. 14 illustrates the entropy generations from mass diffusion over an acoustic period, as the nozzle is placed at different locations. It can be seen that The U-shape distributions of entropy are found at y=120mm. It shrinks into a V-shaped at y=550m. Over the entire acoustic period, the entropy configurations are found to be almost the same. However, dramatic changes are observed as the nozzle is placed at y=400 mm. This is because the nozzle positions y=120mm and 550mm are near the velocity node where the acoustic velocity fluctuation is a minimum. The combustion and flame are stable. When y=400 mm, the nozzle is placed at velocity anti-node, the fluctuations are maximized. Comparing Fig. 14 with Fig. 13 reveals that the mass diffusion entropy generation is less than the heat conduction entropy.

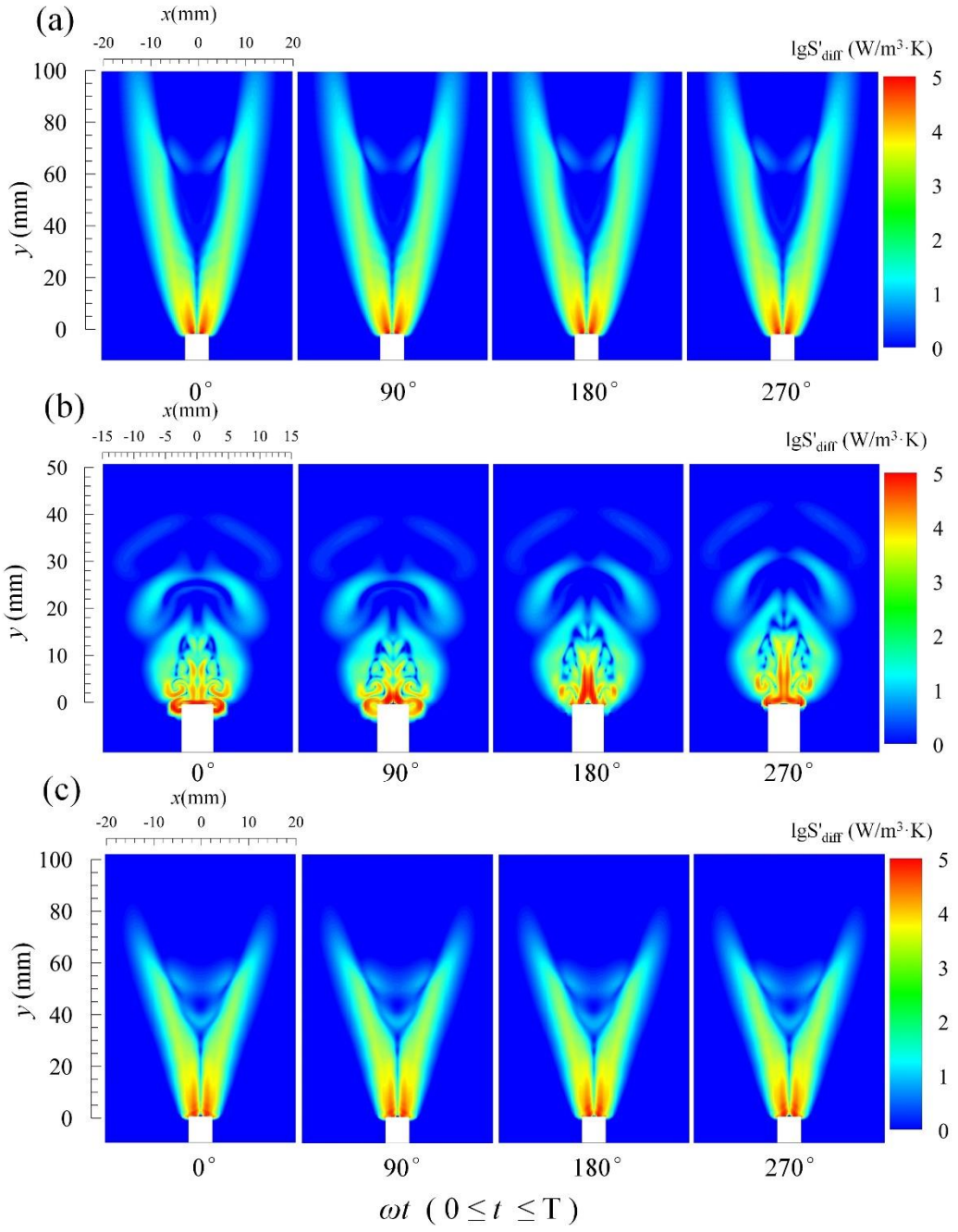

Fig. 14. Contour comparison of volumetric entropy generation resulting from mass diffusion S_{diff} over an acoustic period: nozzle is placed at (a) y=120mm (b) y=400mm (c) y=550mm, as $\bar{u} = 0.15\ m/s$, $u'/\bar{u} = 20\%$, and $\omega/2\pi = 385$Hz.

Fig.15 illustrates the entropy generations resulting from chemical reaction over an acoustic period. The M-shape distributions of entropy are found, when nozzle positions are at 120mm and 550m. The shape is quite different from that of mass diffusion. The entropy generation rate almost do not change in a period. Similar findings are obtained, when the mass diffusion entropy generation is considered as shown in Fig. 14.

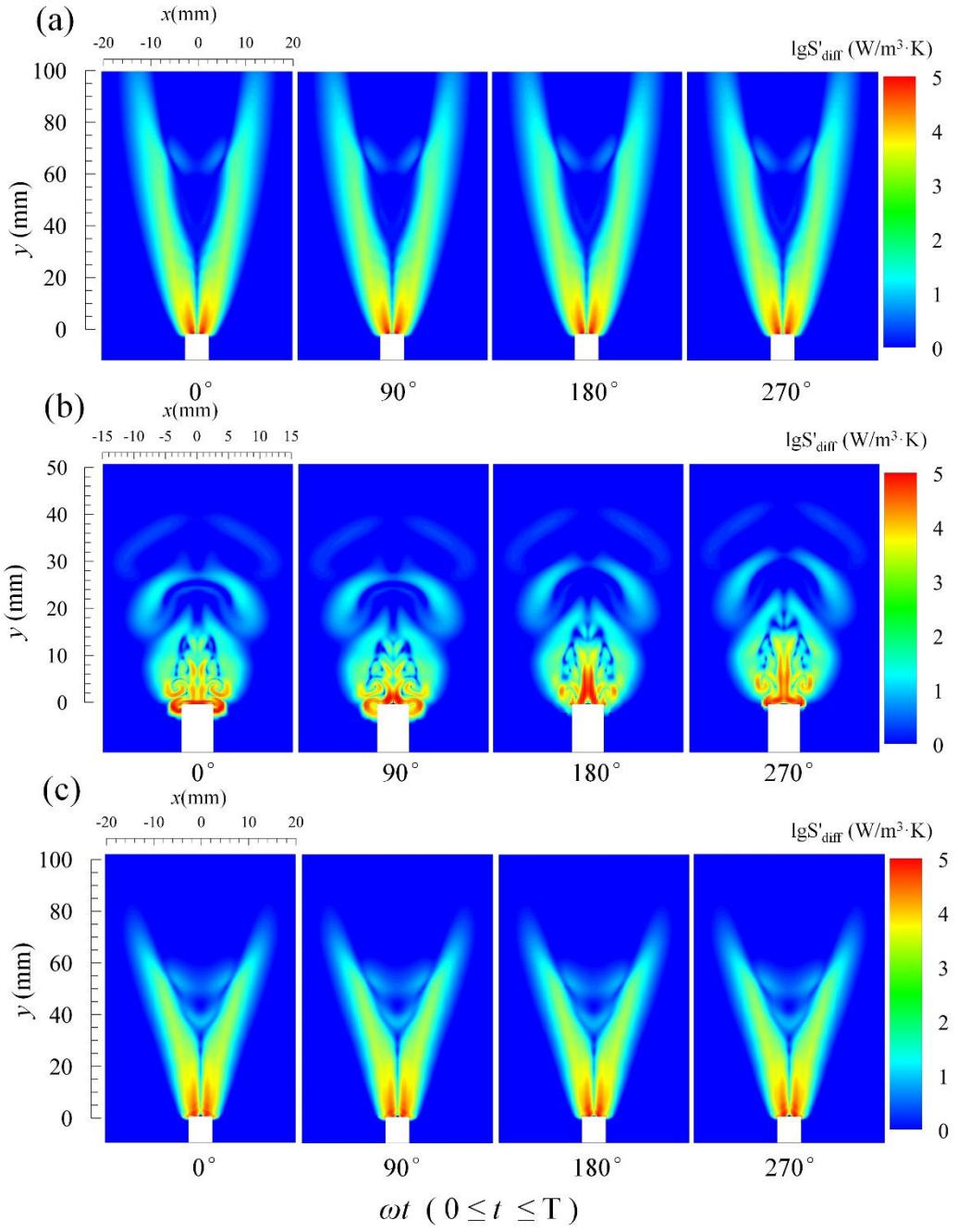

Fig. 15. Contour comparison of volumetric entropy generation resulting from chemical reaction S_{chem} over an acoustic period: nozzle is placed at (a) y=120mm (b) y=400mm (c) y= 550mm, as $\bar{u} = 0.15\ m/s$, $u'/\bar{u} = 20\%$, and $\omega/2\pi = 385$Hz.

Fig.16 (a) and (b) show integrated entropy generation rates and entropy generation induced by these three effects at three frequencies. It is found that the thermal conduction is the dominant player contributing to the total entropy generation. However, the mass diffusion process makes the lowest contribution. When the fuel nozzle is placed axially at y=400mm, the total entropy generation is maximum and the second law efficiency η_{II} is minimum.

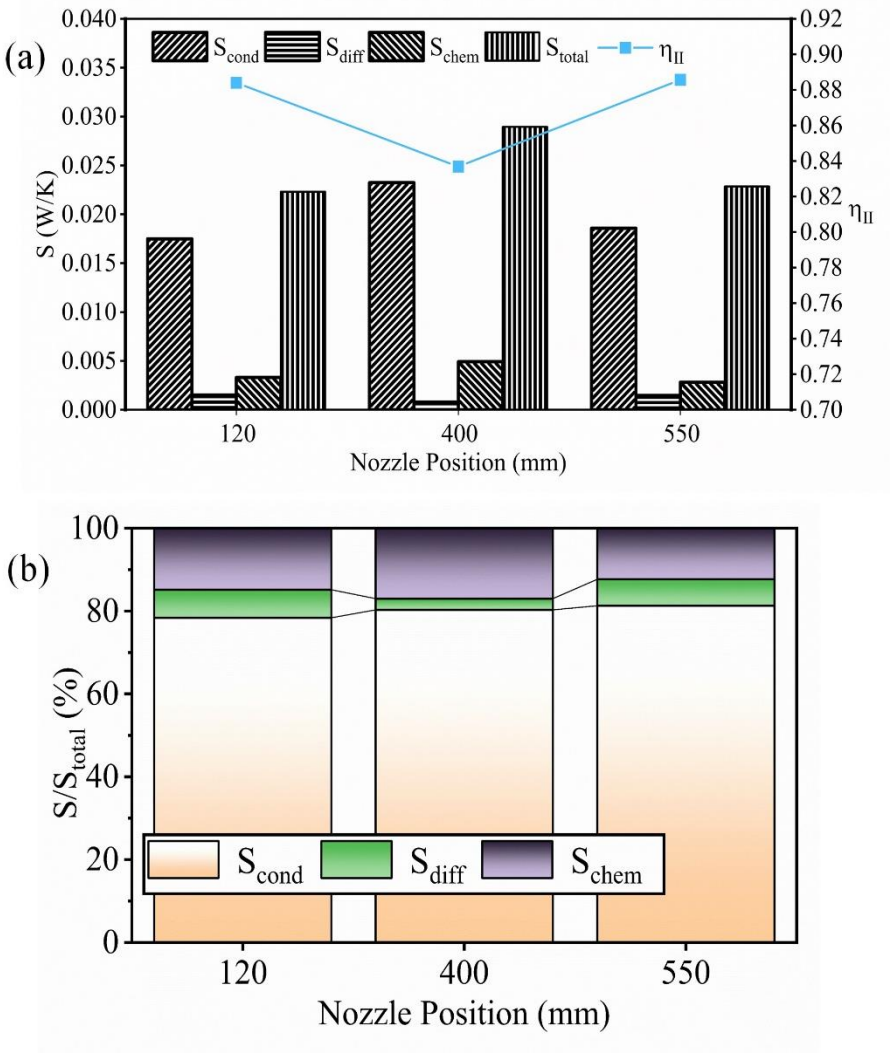

Fig. 16 (a) Volumetric entropy generation rate (S) and the second law efficiency (η_{II}); (b) entropy generation contribution, as the nozzle is placed at three different axial positions.

4.2 Flame transfer function

The flame transfer function is an important description of flame-acoustic interaction [56, 57]. It is widely applied in analyzing thermo-acoustic instability in practical combustors [58-60]. FTF can characterize the relationship between the heat release and the unsteady flow disturbances imposed on the flame [61, 62]. The FTF can be written as:

$$T_F(\omega) = \frac{\hat{Q}(\omega)/\overline{Q}}{\hat{u}(\omega)/\overline{u}} = \|T_F(\omega)\| \cdot e^{j\Phi_F} \tag{18}$$

where $\hat{Q}(\omega)$, $\overline{Q}$, $\hat{u}(\omega)$ and $\overline{u}$ are heat release and velocity in axial direction in frequency domain. Their mean values are denoted by an overbar. $\|T_F(\omega)\|$ represents the gain of FTF and Φ_F is the phase difference between the heat release and oncoming velocity fluctuation. The unsteady velocity is recorded at the location of y = 375 *mm*. The frequency range is from 40 to 600Hz. In addition, the incremental frequency step is 20 Hz.

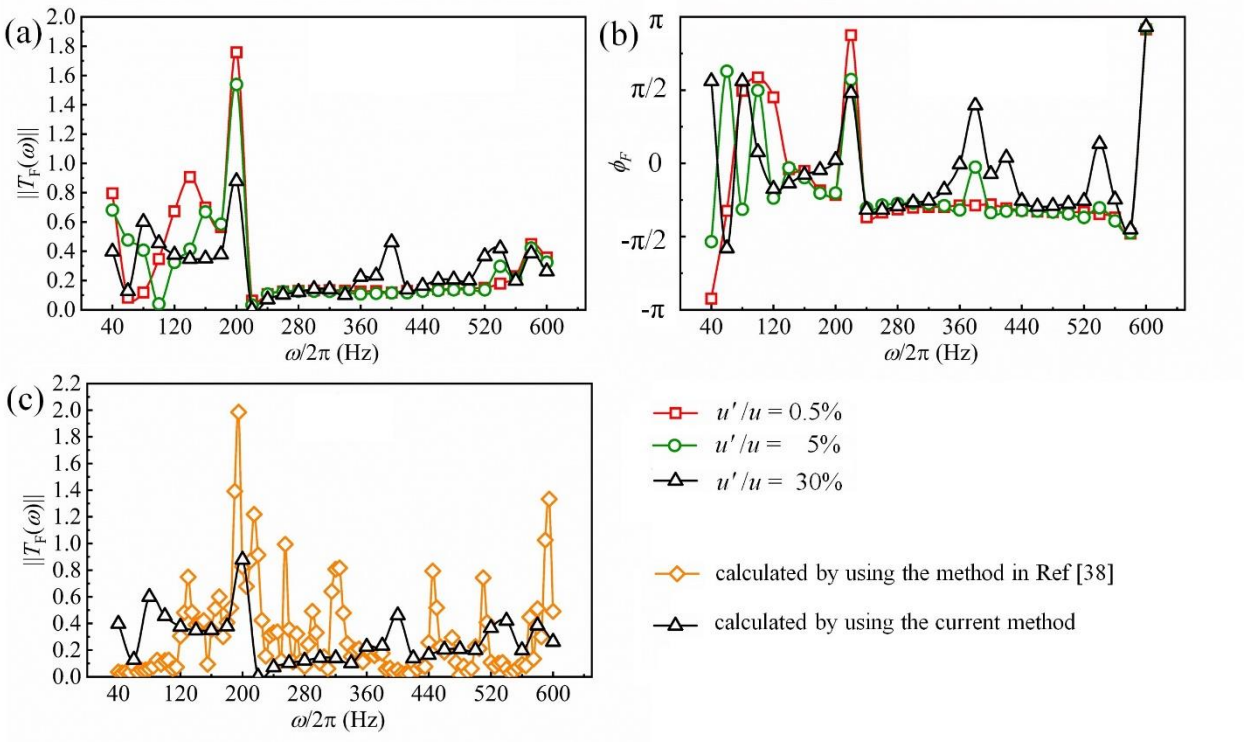

Fig. 17. Variation of the gain and phase of FTF with forcing frequency (40–600 Hz), as $|u'/\bar{u}|$ is set to 3 different values. (a) variation of $\|T_F(\omega)\|$ (b) phase Φ_F, (c) comparison of FTF determined by using the current method and the superimposed sine wave method [38].

The gain of the flame transfer function is shown in Fig.17 (a). The dominant peak of the FTF gain are at 200Hz under three amplitudes. As $|u'/\bar{u}|$ is increased to 30%, local dominant peaks are also found at 400Hz, 540 Hz and 580Hz. Under all three different amplitudes, the minimum gains are found at 220Hz. The peak value of the gain is also varied with increased $|u'/\bar{u}|$. The maximum gain at $|u'/\bar{u}| = 0.5\%$, is approximately 1.76, and decreases with increased $|u'/\bar{u}|$. Fig.17 (b) illustrates the corresponding phase of FTF. It presents the lag between the heat release and oncoming velocity fluctuation. The phase difference is distributed between – π and + π. The calculated flame transfer function shows that the velocity fluctuations at the upstream area near nozzle is sensitive to the acoustic frequencies and amplitudes. Fig. 17(c) compares the flame transfer function calculated by using a current single-tone method and superimposition method proposed by Chen in Ref [38]. It can be seen that there is a reasonably good agreement on the predicted dominant peak at approximately 185 Hz by using these two methods. However, there are more FTF non-harmonic peaks being predicted above 200 Hz. This is quite different from the current prediction. These peaks are most likely due to the round off error of the superimposed sine waves. The classical single-tone acoustic excitation method should be applied in determining FTF in numerical investigations.

5. Conclusions

The present studies consider the entropy generation and flame transfer functions of a jet diffusion flame in a longitudinal standing-wave combustor. 2D time-domain numerical simulations are conducted to gain insights on the dynamic propane- and hydrogen-fueled flame-acoustics interaction in an acoustically resonant tube. The effects of acoustic disturbances frequencies and amplitude, the nozzle axial position are investigated one at a time.

- 3 physical processes: 1) mass diffusion, 2) heat conduction and 3) chemical reaction are identified to contribute to the entropy generation. The dominant player is found to be heat conduction. The mass diffusion is found to play a negligible role on entropy generation.
- As the nozzle axial location is fixed, varying the acoustic frequency does not lead to a dramatic change of the entropy contour over an acoustic period, which results from either mass diffusion, heat conduction or chemical reaction. However, wavy entropy contours at 90 Hz revealing that the acoustic disturbances at a lower frequency strongly distort the flame shape. 200 Hz acoustic disturbances leads to almost the same U-shaped entropy contours. Total entropy generations are maximal and minimal at 385 Hz and 200 Hz respectively, due to the different velocity perturbations as frequencies varying.
- As the acoustic forcing frequency remains unchanged, varying the nozzle location is shown to lead to the entropy contour shapes being changed dramatically from V to U to M. When the nozzle is placed near velocity node, there is minimum total entropy generation. Contour of entropy generation is found to be almost unchanged over an acoustic period and the total entropy generation is minimum. However, when the flame is placed near the velocity anti-node, total entropy generation is maximum. The entropy contour is observed to change dramatically over the period (see Fig. 14(b)).

- Entropy generation can be increased by larger amplitude acoustic excitation. Flame transfer function (FTF) show that the gain of FTF $\|T_F(\omega)\|$ depends strongly on both acoustic excitation amplitude and frequency. Increasing the amplitude of acoustic leads to the flame being more sensitive to the acoustic disturbances over more frequency bands.

Acknowledgments

This work is financially supported by the University of Canterbury, New Zealand with grant No. 452STUPDZ, the National Research Foundation, Prime Minister's Office, Singapore with Grant No. NRF2016NRF-NSFC001-102. This financial support is gratefully acknowledged. Y. Sun would like to thank College of Engineering, University of Canterbury for providing the PhD scholarship.

References

[1] S. Sharma, S.K. Ghoshal. Hydrogen the future transportation fuel: From production to applications. Renewable and Sustainable Energy Reviews, 2015; 43, 1151-1158.

[2] P. Chiesa, G. Lozza, L. Mazzocchi. Using hydrogen as gas turbine fuel. Journal of Engineering for Gas Turbines and Power, 2005; 127(1), 73-80.

[3] C. Acar, I. Dincer, G.F. Naterer. Review of photocatalytic water-splitting methods for sustainable hydrogen production. International Journal of Energy Research, 2016; 40(11), 1449-1473.

[4] B. Khandelwal, A. Karakurt, P.R. Sekaran, V. Sethi, R. Singh. Hydrogen powered aircraft : The future of air transport. Progress in Aerospace Sciences, 2013; 60, 45-59.

[5] H. Nojoumi, I. Dincer, G. Naterer. Greenhouse gas emissions assessment of hydrogen and kerosene-fueled aircraft propulsion. International Journal of Hydrogen Energy, 2009; 34(3), 1363-1369.

[6] J. Park, M.C. Lee. Combustion instability characteristics of H2/CO/CH4 syngases and synthetic natural gases in a partially-premixed gas turbine combustor: Part I—Frequency and mode analysis. International Journal of Hydrogen Energy, 2016; 41(18), 7484-7493.

[7] D. Cecere, E. Giacomazzi, A. Ingenito. A review on hydrogen industrial aerospace applications. International Journal of Hydrogen Energy, 2014; 39(20), 10731-10747.

[8] S.K. Kim, D. Kim, D.J. Cha. Finite element analysis of self-excited instabilities in a lean premixed gas turbine combustor. International Journal of Heat and Mass Transfer, 2018; 120, 350-360.

[9] D. Noh, E. Karlis, S. Navarro-Martinez, Y. Hardalupas, A.M.K.P. Taylor, D. Fredrich, W.P. Jones. Azimuthally-driven subharmonic thermoacoustic instabilities in a swirl-stabilised combustor. Proceedings of the Combustion Institute, 2019; 37(4), 5333-5341.

[10] J. Yoon, M.K. Kim, J. Hwang, J. Lee, Y. Yoon. Effect of fuel-air mixture velocity on combustion instability of a model gas turbine combustor. Applied Thermal Engineering, 2013; 54(1), 92-101.

[11] E. Karlis, Y.S. Liu, Y. Hardalupas, A.M.K.P. Taylor. H-2 enrichment of CH4 blends in lean premixed gas turbine combustion: An experimental study on effects on flame shape and thermoacoustic oscillation dynamics. Fuel, 2019; 254.

[12] S. Li, Q.T. Li, L. Tang, B. Yang, J.Q. Fu, C.A. Clarke, X. Jin, C.Z. Ji, H. Zhao. Theoretical and experimental demonstration of minimizing self-excited thermoacoustic oscillations by applying anti-sound technique. Applied Energy, 2016; 181, 399-407.

[13] G. Ghirardo, M.P. Juniper, M.R. Bothien. The effect of the flame phase on thermoacoustic instabilities. Combustion and Flame, 2018; 187, 165-184.

[14] G. Chen, L.H. Tang, B.R. Mace. Theoretical and experimental investigation of the dynamic behaviour of a standing-wave thermoacoustic engine with various boundary conditions. International Journal of Heat and Mass Transfer, 2018; 123, 367-381.

[15] Z.X. Chen, I. Langella, N. Swaminathan, M. Stohr, W. Meier, H. Kolla. Large Eddy Simulation of a dual swirl gas turbine combustor: Flame/flow structures and stabilisation under thermoacoustically stable and unstable conditions. Combustion and Flame, 2019; 203, 279-300.

[16] J. Kim, M. Jang, K. Lee, A.R. Masri. Experimental study of the beating behavior of thermoacoustic self-excited instabilities in dual swirl combustors. Experimental Thermal And Fluid Science, 2019; 105, 1-10.

[17] T. Lieuwen. Analysis of acoustic wave interactions with turbulent premixed flames. Proceedings of the Combustion Institute, 2002; 29, 1817-1824.

[18] T. Lieuwen. Modeling premixed combustion-acoustic wave interactions: A review. Journal of Propulsion and Power, 2003; 19(5), 765-781.

[19] D. Hwang, K. Ahn, Y. Yoon. Flame Length Scaling of C2H4-Air Premixed Flames under Acoustic Forcing. Journal of Applied Fluid Mechanics, 2018; 11(3), 647-654.

[20] M.K. Kim, J. Yoon, S. Park, M.C. Lee, Y. Yoon. Effects of unstable flame structure and recirculation zones in a swirl-stabilized dump combustor. Applied Thermal Engineering, 2013; 58(1-2), 125-135.

[21] A. Fichera, C. Losenno, A. Pagano. Experimental analysis of thermo-acoustic combustion instability. Applied Energy, 2001; 70(2), 179-191.

[22] A.E.E. Khalil, A.K. Gupta. Acoustic and heat release signatures for swirl assisted distributed combustion. Applied Energy, 2017; 193, 125-138.

[23] A.V. Singh, M. Yu, A.K. Gupta, K.M. Bryden. Thermo-acoustic behavior of a swirl stabilized diffusion flame with heterogeneous sensors. Applied Energy, 2013; 106, 1-16.

[24] S. Farhat, D. Kleiner, Y. Zhang. Jet diffusion flame characteristics in a loudspeaker-induced standing wave. Combustion and Flame, 2005; 142(3), 317-323.

[25] L.W. Chen, Q. Wang, Y. Zhang. Flow characterisation of diffusion flame under non-resonant acoustic excitation. Experimental Thermal And Fluid Science, 2013; 45, 227-233.

[26] L.W. Chen, Y. Zhang. Experimental observation of the nonlinear coupling of flame flow and acoustic wave. Flow Measurement and Instrumentation, 2015; 46, 12-17.

[27] S.M. Camporeale, B. Fortunato, G. Campa. A Finite Element Method for Three-Dimensional Analysis of Thermo-acoustic Combustion Instability. Journal of Engineering for Gas Turbines and Power, 2011; 133(1).

[28] A.P. Dowling, S.R. Stow. Acoustic analysis of gas turbine combustors. Journal of Propulsion and Power, 2003; 19(5), 751-764.

[29] D. Laera, G. Campa, S.M. Camporeale. A finite element method for a weakly nonlinear dynamic analysis and bifurcation tracking of thermo-acoustic instability in longitudinal and annular combustors. Applied Energy, 2017; 187, 216-227.

[30] Y. Xia, D. Laera, W.P. Jones, A.S. Morgans. Numerical prediction of the Flame Describing Function and thermoacoustic limit cycle for a pressurised gas turbine combustor. Combustion Science and Technology, 2019; 191(5-6), 979-1002.

[31] R. Balachandran, B.O. Ayoola, C.F. Kaminski, A.P. Dowling, E. Mastorakos. Experimental investigation of the nonlinear response of turbulent premixed flames to imposed inlet velocity oscillations. Combustion and Flame, 2005; 143(1-2), 37-55.

[32] S. Ducruix, D. Durox, S. Candel. Theoretical, and experimental determinations of the transfer function of a laminar premixed flame. Proceedings of the Combustion Institute, 2000; 28, 765-773.

[33] N. Karimi. Response of a conical, laminar premixed flame to low amplitude acoustic forcing - A comparison between experiment and kinematic theories. Energy, 2014; 78, 490-500.

[34] F. Di Sabatino, T.F. Guiberti, W.R. Boyette, W.L. Roberts, J.P. Moeck, D.A. Lacoste. Effect of pressure on the transfer functions of premixed methane and propane swirl flames. Combustion and Flame, 2018; 193, 272-282.

[35] H.J. Krediet, C.H. Beck, W. Krebs, S. Schimek, C.O. Paschereit, J.B.W. Kok. Identification of the Flame Describing Function of a Premixed Swirl Flame from Les. Combustion Science and Technology, 2012; 184(7-8), 888-900.

[36] L. Tay-Wo-Chong, W. Polifke. Large Eddy Simulation-Based Study of the Influence of Thermal Boundary Condition and Combustor Confinement on Premix Flame Transfer Functions. Journal of Engineering for Gas Turbines and Power, 2013; 135(2).

[37] C.F. Silva, T. Emmert, S. Jaensch, W. Polifke. Numerical study on intrinsic thermoacoustic instability of a laminar premixed flame. Combustion and Flame, 2015; 162(9), 3370-3378.

[38] S. Chen, D. Zhao, H.K.H. Li, T.Y. Ng, X. Jin. Numerical study of dynamic response of a jet diffusion flame to standing waves in a longitudinal tube. Applied Thermal Engineering, 2017; 112, 1070-1082.

[39] K. Nishida, T. Takagi, S. Kinoshita. Analysis of entropy generation and exergy loss during combustion. Proceedings of the Combustion Institute, 2002; 29, 869-874.

[40] A.M. Briones, A. Mukhopadhyay, S.K. Aggarwal. Analysis of entropy generation in hydrogen-enriched methane-air propagating triple flames. International Journal of Hydrogen Energy, 2009; 34(2), 1074-1083.

[41] D.Y. Jiang, W.M. Yang, J.H. Teng. Entropy generation analysis of fuel lean premixed CO/H-2/air flames. International Journal of Hydrogen Energy, 2015; 40(15), 5210-5220.

[42] W. Wang, Z.X. Zuo, J.X. Liu, W.M. Yang. Entropy generation analysis of fuel premixed CH4/H-2/air flames using multistep kinetics. International Journal of Hydrogen Energy, 2016; 41(45), 20744-20752.

[43] D.Y. Jiang, W.M. Yang, K.J. Chua, J.Y. Ouyang, J.H. Teng. Analysis of entropy generation distribution in micro-combustors with baffles. International Journal of Hydrogen Energy, 2014; 39(15), 8118-8125.

[44] M. Safari, M.R.H. Sheikhi. Large eddy simulation-based analysis of entropy generation in a turbulent nonpremixed flame. Energy, 2014; 78, 451-457.

[45] H. Yapici, N. Kayatas, B. Albayrak, G. Basturk. Numerical calculation of local entropy generation in a methane-air burner. Energy Conversion and Management, 2005; 46(11-12), 1885-1919.

[46] J.Q. E, W. Zuo, X.L. Liu, Q.G. Peng, Y.W. Deng, H. Zhu. Effects of inlet pressure on wall temperature and exergy efficiency of the micro-cylindrical combustor with a step. Applied Energy, 2016; 175, 337-345.

[47] J. Wang, C. Du, F. Wu, L. Li, X. Fan. Investigation of the vortex cooling flow and heat transfer behavior in variable cross-section vortex chambers for gas turbine blade leading edge. International Communications in Heat and Mass Transfer, 2019; 108, 104301.

[48] F. Wu, L. Li, J. Wang, X. Fan, C. Du. Numerical investigations on flow and heat transfer of swirl and impingement composite cooling structures of turbine blade leading edge. International Journal of Heat and Mass Transfer, 2019; 144, 118625.

[49] X.J. Fan, C.H. Du, L. Li, S. Li. Numerical simulation on effects of film hole geometry and mass flow on vortex cooling behavior for gas turbine blade leading edge. Applied Thermal Engineering, 2017; 112, 472-483.

[50] A. Fluent. ANSYS Fluent 12.0 user's guide. Ansys Inc, 2009; 15317, 1-2498.

[51] S.Y. Wang, D.B. Ingham, L. Ma, M. Pourkashanian, Z. Tao. Numerical investigations on dynamic stall of low Reynolds number flow around oscillating airfoils. Computers and Fluids, 2010; 39(9), 1529-1541.

[52] D.C. Wilcox. Turbulence modeling for CFD, DCW industries La Canada, CA1998.

[53] L. Umlauf, H. Burchard, K. Hutter. Extending the k-omega turbulence model towards oceanic applications. Ocean Modelling, 2003; 5(3), 195-218.

[54] S.X. Chu, L.H. Liu. Entropy generation analysis of two-dimensional high-temperature confined jet. International Journal of Thermal Sciences, 2009; 48(5), 998-1006.

[55] A. Emadi, M.D. Emami. Analysis of entropy generation in a hydrogen-enriched turbulent non-premixed flame. International Journal of Hydrogen Energy, 2013; 38(14), 5961-5973.

[56] B. Cosic, S. Terhaar, J.P. Moeck, C.O. Paschereit. Response of a swirl-stabilized flame to simultaneous perturbations in equivalence ratio and velocity at high oscillation amplitudes. Combustion and Flame, 2015; 162(4), 1046-1062.

[57] V.K. Rani, S.L. Rani. Development of a comprehensive flame transfer function and its application to predict combustion instabilities in a dump combustor. Combustion Science and Technology, 2018; 190(8), 1313-1353.

[58] Y. Tang, J.K. Zhuo, W. Cui, S.Q. Li, Q. Yao. Non-premixed flame dynamics excited by flow fluctuations generated from Dielectric-Barrier-Discharge plasma. Combustion and Flame, 2019; 204, 58-67.

[59] K.T. Kim, J.G. Lee, B.D. Quay, D.A. Santavicca. Spatially distributed flame transfer functions for predicting combustion dynamics in lean premixed gas turbine combustors. Combustion and Flame, 2010; 157(9), 1718-1730.

[60] R. Bluemner, C.O. Paschereit, K. Oberleithner. Generation and transport of equivalence ratio fluctuations in an acoustically forced swirl burner. Combustion and Flame, 2019; 209, 99-116.

[61] T.L. Kaiser, G. Oztarlik, L. Selle, T. Poinsot. Impact of symmetry breaking on the Flame Transfer Function of a laminar premixed flame. Proceedings of the Combustion Institute, 2019; 37(2), 1953-1960.

[62] A. Chatelier, T. Guiberti, R. Mercier, N. Bertier, B. Fiorina, T. Schuller. Experimental and numerical investigation of the response of a swirled flame to flow modulations in a non-adiabatic combustor. Flow, Turbulence and Combustion, 2019; 102(4), 995-1023.